DRC2/CCDC65 is a central hub for assembly of the nexin–dynein regulatory complex and other regulators of ciliary and flagellar motility

Raqual Bower[a], Douglas Tritschler[a], Kristyn VanderWaal Mills[a], Thomas Heuser[b,c], Daniela Nicastro[b,d], and Mary E. Porter[a,*]

[a]Department of Genetics, Cell Biology, and Development, University of Minnesota Medical School, Minneapolis, MN 55455; [b]Biology Department and Rosenstiel Basic Medical Sciences Research Center, Brandeis University, Waltham, MA 02454; [c]Vienna Biocenter Core Facilities, 1030 Vienna, Austria; [d]Departments of Cell Biology and Biophysics, University of Texas Southwestern Medical Center, Dallas, TX 75390

ABSTRACT The nexin–dynein regulatory complex (N-DRC) plays a central role in the regulation of ciliary and flagellar motility. In most species, the N-DRC contains at least 11 subunits, but the specific function of each subunit is unknown. Mutations in three subunits (DRC1, DRC2/CCDC65, DRC4/GAS8) have been linked to defects in ciliary motility in humans and lead to a ciliopathy known as primary ciliary dyskinesia (PCD). Here we characterize the biochemical, structural, and motility phenotypes of two mutations in the *DRC2* gene of *Chlamydomonas*. Using high-resolution proteomic and structural approaches, we find that the C-terminal region of DRC2 is critical for the coassembly of DRC2 and DRC1 to form the base plate of N-DRC and its attachment to the outer doublet microtubule. Loss of DRC2 in *drc2* mutants disrupts the assembly of several other N-DRC subunits and also destabilizes the assembly of several closely associated structures such as the inner dynein arms, the radial spokes, and the calmodulin- and spoke-associated complex. Our study provides new insights into the range of ciliary defects that can lead to PCD.

INTRODUCTION

Cilia and flagella are microtubule-based organelles that play essential roles in human health and development, serving both as sensory antennae and as motile structures. Defects in the assembly, signaling, or motility of these organelles have severe consequences for an organism, and lead to a diverse spectrum of diseases known as ciliopathies in humans (reviewed in Mitchison and Valente, 2017; Reiter and Leroux, 2017). Ciliary and flagellar motility are critical for the clearance of mucus and foreign particles from the respiratory tract, fertilization in the reproductive tract, circulation of fluid in the brain and spinal cord, and the determination of the left–right body axis during embryonic development. Genomic and proteomic approaches have identified more than 600 polypeptides as structural subunits of the ciliary axoneme, and several other proteins contribute to the assembly and transport of these components into the axoneme (Li *et al.*, 2004; Pazour *et al.*, 2005; Ishikawa *et al.*, 2012; Blackburn *et al.*, 2017). Advances in the development of high-resolution structural techniques, combined with the highly ordered and repetitive nature of axoneme structure, have yielded insights into the location and interactions of several polypeptides (reviewed in Mizuno *et al.*, 2012), but thus far only a fraction of the ciliary proteins have been clearly correlated with a specific structure and/or function.

Most motile cilia and flagella contain nine outer doublet microtubules arranged in a ring that surrounds two singlet microtubules in the central pair (CP) to form the 9 + 2 axoneme. The outer and inner

Abbreviations used: CP, central pair; CSC, calmodulin- and spoke-associated complex; DHC, dynein heavy chain; DIC, differential interference contrast; ET, electron tomography; FAP, flagellar associated polypeptide; GFP, green fluorescent protein; HA, hemagglutinin; IC, intermediate chain; IDA, inner dynein arm; IFT, intraflagellar transport; iTRAQ, isobaric tag for relative and absolute quantitation; LC, light chain; MS, mass spectrometry; N-DRC, nexin–dynein regulatory complex; ODA, outer dynein arm; PCD, primary ciliary dyskinesia; PEET, particle estimation for electron tomography; *pf*, paralyzed flagella; RS, radial spoke; RS3S, radial spoke 3 stump; RSP, radial spoke protein; TAP, Tris-acetate-phosphate; TEM, transmission electron microscopy; TIRF, total interference reflection fluorescence; WT, wild type.

dynein arms (ODA and IDA) are large, multisubunit motor proteins that drive interdoublet sliding (Gibbons, 1965), and they form two distinct rows along the length of the A-tubule of each outer doublet. Both the ODAs and IDAs walk along the surface of the B-tubule of the neighboring outer doublet in an ATP-sensitive manner, pushing the adjacent doublets toward the tip of the axoneme (Satir, 1968). In an intact cell, the outer doublet microtubules are attached to basal bodies at their minus ends, and the outer doublets are also cross-linked by nexin links every 96 nm along their length. These structures limit the extent of interdoublet sliding and convert microtubule sliding into axonemal bending. However, given that all dyneins are minus-end–directed motors, the geometry of the axoneme dictates that the site of dynein activity must switch between opposite sides of the axoneme for effective bending to occur (Sale and Satir, 1977; Satir, 1985; Fox and Sale, 1987). In addition, most organisms can modify the pattern of axonemal bending in response to internal or external stimuli.

The study of motility mutants in the unicellular alga *Chlamydomonas* has identified several axonemal complexes as important regulators of dynein activity and flagellar motility, such as the CP microtubules and the radial spokes (RS) that transmit signals from the CP projections to the dynein arms on the outer doublet microtubules (reviewed in Smith and Yang, 2004). Mutants that lack either the CP or the RS are often paralyzed, and the velocity of dynein-driven sliding in sliding–disintegration assays is also reduced (Witman *et al.*, 1978; Smith and Sale, 1992; Smith 2002). The prevailing model is that the projections of the CP microtubules make contact with the RS in an asymmetric manner during flagellar bending. These signals are then transduced through the RS to regulatory complexes located at the base of the RS to coordinate the activity of the multiple dynein motors (Smith and Yang, 2004). The study of extragenic suppressors that restore limited motility to paralyzed CP/RS mutants has identified two of these regulatory complexes (Huang *et al.*, 1982). The first is the intermediate chain/light chain (IC/LC) complex of the two-headed I1 dynein, which is located at the proximal end of the 96-nm repeat, at the junction between the base of RS1, several IDAs, the MIA complex, and the row of ODAs (Bower *et al.*, 2009; Heuser *et al.*, 2012a; Yamamoto *et al.*, 2013). The second is the nexin–dynein regulatory complex (N-DRC), which is located at the distal end of the 96-nm repeat, at the junction between the bases of RS2 and the shorter RS3S, several other IDAs, the calmodulin- and spoke-associated complex (CSC), and the row of ODAs (Mastronarde *et al.*, 1992; Piperno *et al.*, 1992; Gardner *et al.*, 1994; Heuser *et al.*, 2009, 2012b).

The N-DRC is a large 1.5-MDa structure composed of at least 11 distinct subunits (Heuser *et al.*, 2009; Lin *et al.*, 2011; Bower *et al.*, 2013). It contains a base plate that attaches to the surface of the outer doublet, beginning at the inner junction between the A- and B-tubule and wrapping around the A-tubule to protofilament A4, and a linker that extends across the interdoublet space to the adjacent B-tubule. Both the base plate and the linker make contacts with other substructures on the outer doublet (Heuser *et al.*, 2009). The precise arrangement of the 11 subunits in the structure of the N-DRC is unknown, but recent work with epitope-tagged subunits has revealed the approximate locations of DRC1-5. The C-termini of DRC1, DRC2, and DRC4 are located in the base plate, near the A- and B-tubule inner junction, and the N-termini extend through the linker toward the neighboring B-tubule (Oda *et al.*, 2015; Song *et al.*, 2015). DRC3 and DRC5 are located in the linker region (Awata *et al.*, 2015; Oda *et al.*, 2015; Song *et al.*, 2015). Mutations in individual DRC subunits have diverse phenotypes (Table 1). *drc3* and *drc5 (sup-pf4)* mutations have limited impact on the assembly of

other DRC subunits and subtle effects on motility (Huang *et al.*, 1982; Awata *et al.*, 2015), whereas *drc1 (pf3)* and *drc4 (pf2, sup-pf3)* mutations have more dramatic effects on motility and the assembly of other DRC subunits and associated IDAs (Gardner *et al.*, 1994; Piperno *et al.*, 1994; Heuser *et al.*, 2009; Lin *et al.*, 2011; Bower *et al.*, 2013; Wirschell *et al.*, 2013).

Defects in the assembly of the ODAs, IDAs, CP projections, RS, and N-DRC have been linked to ciliary motility defects and primary ciliary dyskinesia (PCD) in human patients (reviewed in Mitchison and Valente, 2017). However, detailed characterization of biochemical and structural defects in human cilia is challenging due to the limited quantity of purified material available for analysis. In these cases, comparative studies of mutant phenotypes in model organisms have proven to be valuable in determining the likely impact of a given disease-causing mutation. For example, PCD mutations have been identified in DRC1/CCDC164 and DRC4/GAS8, and analysis of the motility, biochemical, and structural phenotypes observed with related *drc* mutations in *Chlamydomonas* has provided insights into the defects that lead to human disease (Wirschell *et al.*, 2013; Olbrich *et al.*, 2015; Jeanson *et al.*, 2016; Lewis *et al.*, 2016). PCD mutations have also been identified in CCDC65, the human orthologue of DRC2, but in *Chlamydomonas*, DRC2 is linked to an inner arm motility mutant known as *ida6* (Austin-Tse *et al.*, 2013; Horani *et al.*, 2013). The *ida6* mutant was first described as a slow-swimming strain with a defect in the assembly of single IDA known as dynein e (Kato *et al.*, 1993). Identification of *ida6* as a *drc2* mutation prompted a reevaluation of axoneme structure by thin section transmission electron microscopy (TEM). The two-dimensional (2D) averaging of longitudinal images revealed the loss of a crescent-shaped structure above RS2, similar to that seen in previous images of other *drc* mutants (Austin-Tse *et al.*, 2013).

To obtain more complete information about the function of DRC2 and its role in the assembly of the N-DRC and IDAs, we have characterized the molecular, biochemical, and structural phenotypes of two *drc2* mutations in detail. First, we generated and characterized several epitope-tagged strains for analysis of N-DRC assembly in vivo and in vitro. We then used iTRAQ labeling, quantitative mass spectrometry, and spectral counting to identify the polypeptide defects in mutant axonemes and more precisely define the IDAs most closely associated with the N-DRC. Finally, we employed high-resolution cryo-ET and classification analysis to more rigorously describe the structural defects in *drc2/ida6* mutant axonemes and to compare *drc2/ida6* with another closely related *n-drc* mutant, *drc1/pf3*. These studies reveal the importance of both DRC1 and DRC2 in stabilizing interactions between the N-DRC base plate, multiple IDAs, the RS, and the CSC. They also indicate how defects in DRC1 and DRC2 can lead to such profound changes in ciliary motility in other organisms and result in PCD.

RESULTS

sup-pf5 is a *drc2* mutation

We previously identified DRC2 as the mutant gene product of the *IDA6* locus (Austin-Tse *et al.*, 2013). However, there is little information about the impact of a defective DRC2 subunit (also known as FAP250) on the assembly of other axonemal proteins in the *ida6* strain. The *ida6* mutation is caused by a single nucleotide substitution in the stop codon and is predicted to add 101 amino acids to the C-terminus of the DRC2 polypeptide, but the resulting protein is not assembled into the axoneme (Figure 1, A and B; see also Austin-Tse *et al.*, 2013). The *sup-pf5* mutant is a slow-swimming strain that was isolated as an extragenic suppressor of paralyzed RS/CP mutants (Piperno *et al.*, 1992). The *sup-pf5* mutation is a

	Size (kDa)	Wild-type	pf3 (drc1)	sup–pf5 (drc2)	ida6 (drc2)	drc3	sup–pf3 (drc4)	pf2 (drc4)	sup–pf4 (drc5)
N–DRC subunit[a]									
DRC1	79	+	–	–	–	+	+	+	+
DRC2	65	+	–	–	–	+	+	+	+
DRC3	60	+	±	±	±	–	±	–	+
DRC4	55	+	+	+	+	+	±	–	+
DRC5	43	+	–	–	–	+	–	–	–
DRC6	28	+	–	ND	–	+	–	–	–
DRC7	177	+	±	±	±	+	±	–	+
DRC8	19	+	±	–	±	+	±	±	+
DRC9	46	+	±	ND	±	+	±	±	+
DRC10	41	+	±	ND	±	+	ND	±	ND
DRC11	95	+	–	–	–	+	–	–	+
Monomeric dyneins[b]		+	±	±	±	ND	±	±	+
Dynein a/DHC6		+	+	ND	±	ND	+	+	+
Dynein b/DHC5		+	+	ND	+	ND	+	+	+
Dynein c/DHC9		+	±	ND	±	ND	+	+	+
Dynein d/DHC2		+	±	ND	±	ND	+	±	+
Dynein e/DHC8		+	–	–	–	ND	±	±	+
Dynein g/DHC7		+	±	ND	±	ND	+	+	+
Actin		+	±	±	±	ND	+	±	+
Centrin		+	±	±	ND	ND	+	±	+
p28		+	±	±	±	ND	±	±	+
p38		+	±	ND	±	ND	ND	ND	ND
p44		+	±	ND	±	ND	ND	ND	ND
Other polypeptides									
CaM–IP3 (FAP61)[c]		+	±	±	±	ND	+	+	+
Tektin[d]		+	–	–	–	ND	+	+	+

[+]Present at WT levels; –, not detected; ±, reduced; ND = not determined.
[a]DRC subunit data compiled from Huang *et al.*, 1982; Piperno *et al.*, 1992, 1994; Lin *et al.*, 2011; Bower *et al.*, 2013; Wirschell *et al.*, 2013; Awata *et al.*, 2015; this study.
[b]Dynein subunit data compiled from Piperno *et al.*, 1992, 1994; Kato *et al.*, 1993; Piperno, 1995; Gardner *et al.*, 1994; Bui *et al.*, 2012; Bower *et al.*, 2013; Wirschell *et al.*, 2013; this study.
[c]CaM–IP3 data compiled from Bower *et al.*, 2013; Wirschell *et al.*, 2013; this study.
[d]Tektin data compiled from Yanagisawa and Kamiya, 2004; Austin–Tse *et al.*, 2013; Wirschell *et al.*, 2013; this study.

TABLE 1: Polypeptide defects observed in *n–drc* mutants.

single-base-pair change (TG**G** to TG**A**) in exon 7 that results in a premature stop codon that is predicted to truncate DRC2 at amino acid 291 in the middle of the protein, specifically in the third coiled-coil domain (Figure 1, B–D). Western blot analysis confirmed that DRC2 is truncated and significantly reduced in *sup-pf5* axonemes (Figure 1E). As the site of the *sup-pf5* mutation is close to the site of a disease-causing mutation in the human orthologue, CCDC65 (Figure 1D; Austin-Tse *et al.*, 2013), a better understanding of the *drc2* mutant phenotypes should provide insights into the range of defects that result in PCD.

Rescue of ida6 and sup-pf5 with epitope-tagged DRC2
We showed previously that DRC4 and DRC5 are distributed along the length of the flagella and near the basal body region in *Chlamydomonas* cells (Rupp and Porter, 2003; Bower *et al.*, 2013). To de-

termine the distribution of DRC2, we transformed *ida6* and *sup-pf5* with HA- and GFP-tagged constructs of the wild-type (WT) *DRC2* gene (Figure 1B) and screened for transformants with WT motility. As expected, DRC2-GFP and DRC2-HA were found along the length of the flagella and in the basal body region (Figure 2, A and B). Measurements of flagellar motility showed that the epitope-tagged *DRC2* constructs rescued both strains and increased swimming velocities to near WT levels (Figure 2, C and D).

To determine the impact of *drc2* mutations on the assembly of other DRC subunits, we analyzed isolated axonemes from WT, mutant, and rescued strains on Western blots. As shown in Figure 2E, DRC2 migrated at ~65 kD in WT and the *DRC2*-rescued strain but could not be detected in *ida6*, similar to previous results (Austin-Tse *et al.*, 2013). However, both DRC2-GFP and DRC2-HA assembled into the axoneme in rescued strains and migrated at positions
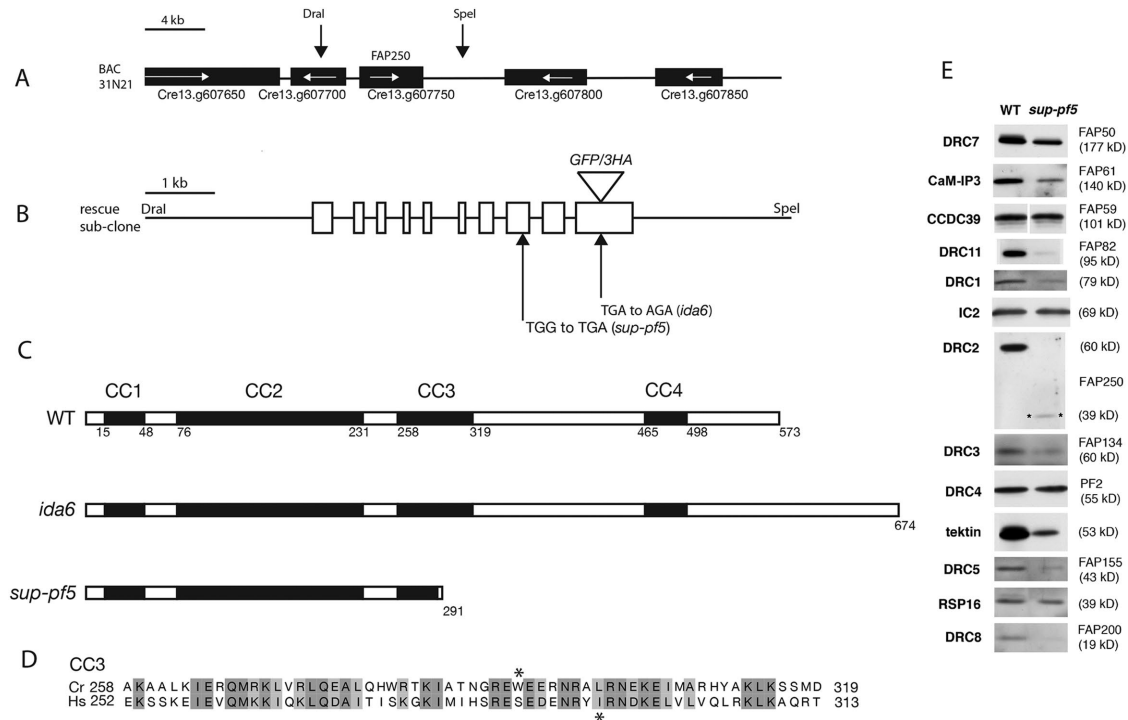
DRC2 connects several axoneme structures |

FIGURE 1: Both *ida6* and *sup-pf5* are *drc2* mutations. (A) Diagram of genes contained within BAC clone 31N21. This clone was digested with *Dra*I and *Spe*I to release a genomic fragment encoding DRC2 (FAP250). (B) Diagram of the subclone containing DRC2 showing the location of the *sup-pf5* and *ida6* mutations and the site of the HA or GFP epitope tags. (C) Diagram of the predicted secondary structure of the DRC2 polypeptide showing the four coiled-coil domains in the wild-type (WT) sequence, the addition of 101 amino acids to the C-terminus of the *ida6* sequence, and the truncation of the third coiled-coil domain in the *sup-pf5* sequence. (D) The aligned amino acid sequences of the third coiled-coil domains in the *Chlamydomonas* (Cr) and *Homo sapiens* (Hs) DRC2 polypeptides. The asterisks indicate the site of the *Chlamydomonas sup-pf5* mutation (top) and the *H. sapiens* mutation (bottom) linked to PCD by Austin-Tse *et al.* (2013). (E) Western blot of WT and *sup-pf5* axonemes probed with antibodies to different polypeptides reveals that truncation of DRC2 (indicated by an asterisk in the DRC2 panel) reduces the assembly of multiple N-DRC subunits, the CSC (FAP61), and tektin, but does not alter assembly of ODA subunits (IC2/IC69), RS subunits (RSP16), or the molecular ruler CCDC39 (FAP59).

consistent with the predicted sizes of the epitope-tagged polypeptides (Figure 2E). Similar results were observed with DRC2-HA subunits in *sup-pf5* rescued strains (Figure 2F). When the region of the blot containing the truncated DRC2 subunit (DRC2*) was overexposed, the mutant band was easily detected in *sup-pf5*, but reduced in the five *DRC2-HA* strains, demonstrating that DRC2-HA displaced the truncated DRC2* subunits in the axonemes of the rescued strains.

The absence or truncation of DRC2 in *ida6* and *sup-pf5* also correlated with a decrease in the assembly of at least two other axonemal polypeptides, DRC1 and tektin (Figures 1E and 2, E and F; see also Austin-Tse *et al.*, 2013). Both DRC1 and tektin were restored to WT levels in the *DRC2*-rescued strains (Figure 2, E and F). However, we did not observe a major decrease in the amount of DRC4 in either mutant (Figures 1E and 2, E and F). These results suggested that *drc2* mutations might alter the assembly of a different group of polypeptides than *drc4* mutations (Bower *et al.*, 2013). These observations also raised the possibility that the pathway of assembly for DRC2 might differ from that previously described for DRC4 (Bower *et al.*, 2013; Wren *et al.*, 2013). To test the first hypothesis, we compared the polypeptide composition of WT, mutant, and rescued axonemes by iTRAQ labeling and tandem mass spectrometry (see below). To determine if the pathway for DRC2 assembly might be different from that for DRC4 assembly, we analyzed the time course of DRC2-GFP assembly into the flagella using dikaryon rescue.

Assembly and turnover of DRC2 subunits in dikaryon flagella

The dikaryon rescue experiments are shown in Figure 2, G and H. Cells expressing DRC2-GFP were mated to unlabeled WT cells or *ida6* cells to form quadriflagellate dikaryons, fixed at various time points after mating, and then analyzed by immunofluorescence for the appearance of GFP signal in the two flagella of the unlabeled cells. When *DRC2-GFP* cells were mated to WT cells, very little GFP signal could be detected in the two flagella from the WT parent, even 1 h after mating (Figure 2G). Turnover of endogenous DRC2 in WT flagella is therefore relatively slow compared with the time course of intraflagellar transport (IFT) of DRC2-GFP subunits observed by TIRF microscopy (Wren *et al.*, 2013). In contrast, when *DRC2-GFP* cells were mated to *ida6* cells, a strong GFP signal could be detected along the length of both flagella from the *ida6* parent within 30 min (Figure 2H). DRC2-GFP can therefore assemble onto vacant sites in *ida6* axonemes shortly after transport into the axoneme, even in the presence of endogenously bound DRC4 subunits. Similar results were previously observed in dikaryon rescue experiments with DRC4-GFP in the presence of bound DRC2 (Bower *et al.*, 2013). Taken together, the differences in DRC subunit turnover in WT and mutant flagella suggest that DRC2 and DRC4 may be assembled and/or transported as part of distinct subcomplexes in living cells.

Characterization of DRC2 associated proteins by iTRAQ analysis and quantitative mass spectrometry

To more completely characterize the polypeptide defects in the *drc2* mutants and compare them with other *drc* mutants, we isolated axonemes from WT, mutant, and rescued strains and subjected them to iTRAQ labeling and tandem mass spectrometry (MS/MS) using an improved protocol (see *Materials and Methods* for details). This approach makes it possible to compare complex protein mixtures and identify a small subset of polypeptides that are quantitatively different between samples (Portman *et al.*, 2009; Bower *et al.*, 2013; Reck *et al.*, 2016). In the first experiment, duplicate samples of WT, *ida6*, *DRC2-HA*, and *pf3* axonemes were digested with trypsin, labeled with eight different iTRAQ tags, and then mixed together. The *pf3* sample was included because previous work had shown that DRC2 is also reduced in this strain (Lin *et al.*, 2011; Bower *et al.*, 2013; see Table 1). The *pf3* mutation has been identified as a premature stop in the transcript encoding the DRC1 subunit of the N-DRC (Wirschell *et al.*, 2013). The pooled iTRAQ mixture was first fractionated by liquid chromatography and then loaded into a mass spectrophotometer. A total of 481 proteins were identified with high confidence at a false discovery rate of 5% in the 8-plex experiment, and for most proteins, no significant differences were observed between the WT and *ida6* samples. However, a small number of proteins were reproducibly reduced in *ida6* and the closely related *drc1* mutant *pf3* and restored to WT levels in the *DRC2-HA* rescued sample (Tables 1 and 2).

To increase the number of proteins detected at high confidence, we repeated the iTRAQ analysis using duplicate samples of *ida6* and the *DRC2-HA* rescued strain and labeled these samples with four different iTRAQ labels. A total of 1089 proteins were identified in the second 4-plex experiment, but again only a small number were reproducibly reduced in *ida6* compared with the rescued strain (Table 2). Based on the iTRAQ analysis, the proteins most significantly reduced in *ida6* and *pf3* axonemes are those previously identified to be associated with the N-DRC complex, DHC8, and tektin (Table 2). In addition, four RS-associated proteins (RSP8, FAP206, FAP251/CaM-IP4, FAP91/CaM-IP2) and three other polypeptides (FAP241, FAP273, and Cre09.g397993) were decreased. However, most RS proteins or other doublet microtubule-associated proteins were not consistently altered in a statistically significant manner ($p < 0.05$).

To confirm and extend these observations, we probed Western blots of axonemes isolated from WT, *ida6*, *DRC2-HA*, and *pf3* with antibodies to N-DRC subunits. DRC1, DRC2, DRC5, DRC8, and DRC11 were barely detected in *ida6* and *pf3* axonemes, and DRC3, DRC4, and DRC7 were reduced to varying degrees (Figure 3A). Similar results were observed with *sup-pf5* axonemes (Figure 1E). The signals observed on the blots were consistent with the protein ratios predicted by iTRAQ analysis (Table 2). Probing the blots with antibodies for subunits of the outer dynein arms (IC2/IC69), the I1 inner arm dynein (IC140), and the radial spokes (RSP16) confirmed that these proteins were unchanged in all samples, consistent with the iTRAQ results (Figures 1E and 3A and Table 2). Although the *ida6* and *sup-pf5* mutations affect different regions of the DRC2 polypeptide, the two mutations have similar consequences for the assembly of other DRC subunits. The defects seen in *ida6* and *sup-pf5* are also very similar to those observed in the *drc1* mutant, *pf3* (Figure 3A; see also Lin *et al.*, 2011; Wirschell *et al.*, 2013), and far more severe than those observed in *pf2*, *sup-pf3*, *drc3*, and *sup-pf4* (Table 1; Piperno *et al.*, 1994; Lin *et al.*, 2011; Bower *et al.*, 2013; Awata *et al.*, 2015).

To confirm that the defects observed in *ida6* were the result of a failure to assemble N-DRC subunits onto the axoneme and not an indirect effect on the stability of N-DRC subunits in the cytoplasm, we also analyzed whole-cell lysates on Western blots (Figure 3B). Probing WT and *ida6* lysates with the DRC2 antibody demonstrated that the *ida6* mutation (which adds an additional 101 amino acids to the C-terminus of the DRC2 sequence) dramatically reduced the amount of DRC2 protein in the cytoplasm. Probing a duplicate blot with a DRC1 antibody revealed that the DRC1 protein was also reduced in *ida6* lysates. Duplicate blots probed with antibodies to several other DRC subunits (DRC5, DRC7, and DRC11) showed that the cytoplasmic levels of these proteins were unaffected by the *ida6* mutation. These results suggest that DRC1 and DRC2 form a subcomplex in the cytoplasm prior to assembly into the axoneme. However, the presence or absence of this subcomplex does not affect the stability of the other N-DRC subunits.

Because *ida6* was originally identified as an inner arm motility mutant defective in assembly of dynein e (Kato *et al.*, 1993), we tested several other motility mutants for possible defects in assembly of N-DRC subunits. The *pf28/oda2* mutation in the γ DHC disrupts the assembly of the ODAs (Mitchell and Rosenbaum, 1985). In contrast, the assembly of different subsets of IDAs is disrupted in the inner arm mutants *ida2*, *ida4*, *ida5*, and *IO* (Huang *et al.*, 1979; Kamiya *et al.*, 1991; Kato *et al.*, 1993, Yamamoto *et al.*, 2017), including some of the DHCs affected in *ida6* (see below). The *pf14* mutation disrupts the assembly of the RS (Huang *et al.*, 1977), and *mbo2* and *pf12* disrupt the assembly of beak structures in outer doublets #5 and #6 (Segal *et al.*, 1984; Tam and Lefebvre, 2002). No defects in the assembly of N-DRC subunits were detected in any of these strains (Figure 3B). Thus, the *drc2* mutants *ida6* and *sup-pf5* are more similar to the *drc1* mutant *pf3* than any other motility mutants.

Given the numerous connections that the N-DRC makes with other structures in the axoneme (Heuser *et al.*, 2009, 2012b), we analyzed the iTRAQ data to identify other components that could potentially interact with the N-DRC subunits. As expected, DHC8 was significantly reduced in both *ida6* and *pf3*, but several DHCs were not detected or not consistently altered in either iTRAQ experiment. Because the DHCs are extremely large polypeptides that vary widely in abundance, their dynamic range can make it challenging to interpret the ratios obtained from different iTRAQ experiments against the background of other axonemal proteins. We therefore reanalyzed the DHC content of the axonemes more directly using SDS–PAGE and spectral counting (Zhu *et al.*, 2010; Bower *et al.*, 2013). WT, *ida6*, *DRC2-HA*, and *DRC2-GFP* axonemes were fractionated by SDS–PAGE, and the high-molecular-weight region was excised from gel to enrich for DHCs relative to other proteins in the axonemes (Bower *et al.*, 2013; Wirschell *et al.*, 2013). Each sample was extracted and digested with trypsin, and four replicates per sample were analyzed by tandem mass spectrometry to determine the total number of assigned spectra for each DHC. Because the two I1 DHCs were constant between samples, the total number of assigned spectra for each DHC was normalized relative to the total number of assigned spectra for the I1 DHCs. The results are shown in Figure 4A, and the relative abundance of each DHC in the four samples is expressed as a percentage of the I1 DHCs present. No significant differences in DHC3, DHC4, or DHC5 were observed between the four strains. As expected, DHC8 was missing in *ida6* (Kato *et al.*, 1993) but restored to WT levels in the rescued strains. DHC2, DHC6, DHC7, and DHC9 were reduced to varying degrees in *ida6* and restored to WT levels in the rescued strains. In contrast, DHC11 was elevated in *ida6* but decreased to WT levels in
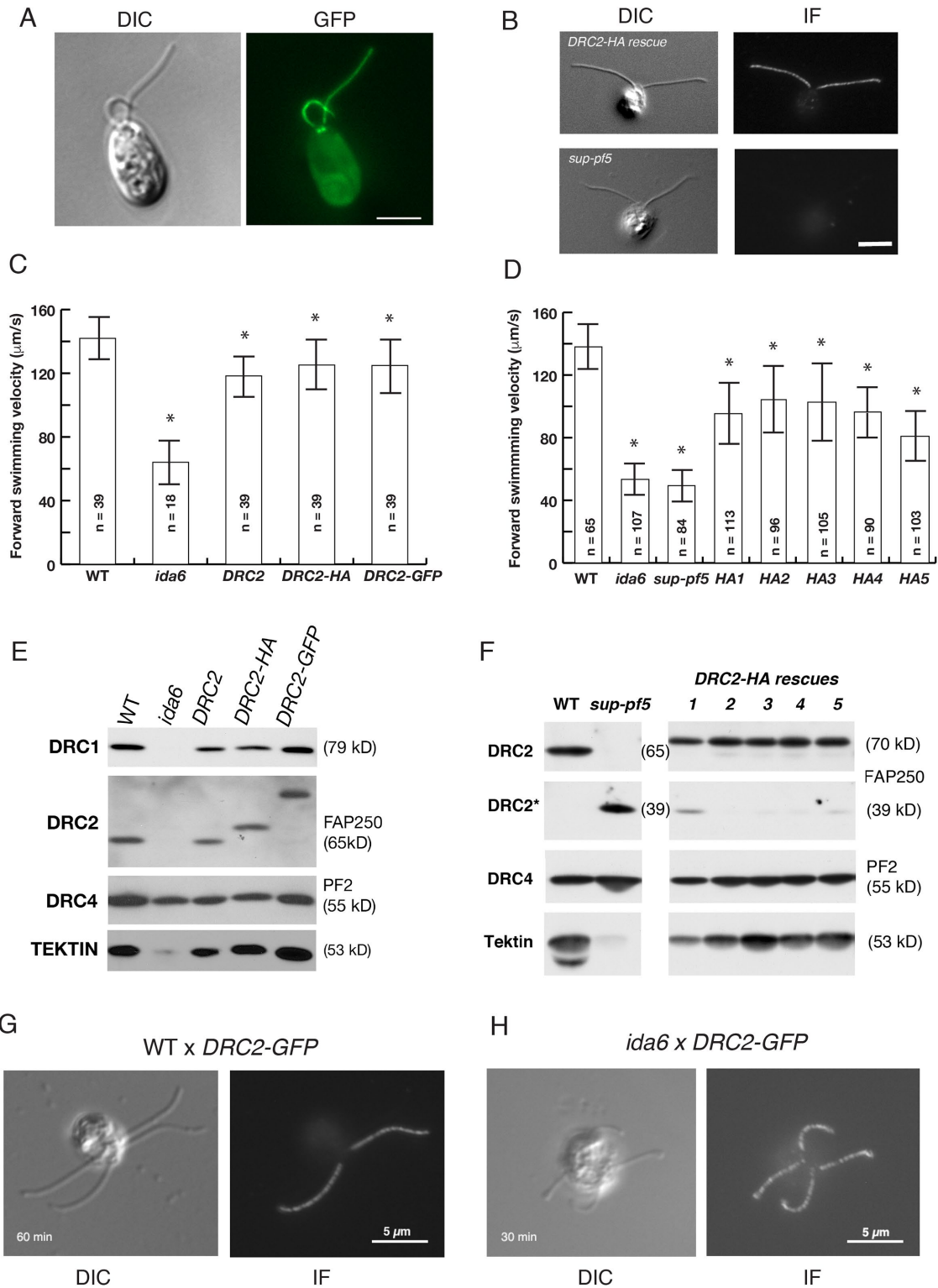
FIGURE 2: Transformation with HA- or GFP-tagged *DRC2* rescues *ida6* and *sup-pf5*. (A) Live cell images of an *ida6* strain rescued with *DRC2-GFP* transgene as viewed by DIC (left) or confocal (right) microscopy show the distribution of DRC2 in the basal body region and along the length of both flagella. (B) Images of a fixed *sup-pf5* cell (bottom) or *DRC2-HA* rescued cell (top) stained with an antibody to the HA epitope tag as viewed by DIC (left) or fluorescence (right) microscopy demonstrate the presence of DRC2-HA in the flagella of the rescued strain. The basal body region is out of the plane of focus in this image. (C, D) Measurements of motility as viewed by phase contrast microscopy indicate that transformation of either *ida6* (C) or *sup-pf5* (D) with WT or epitope-tagged *DRC2* transgenes increased forward swimming velocities to near WT levels. All strains indicated by asterisks were slower than WT, but the *DRC2* rescued strains were significantly faster than *ida6* or *sup-pf5* ($p < 0.05$). (E, F) Western blots of axonemes from WT, mutant, and rescued strains were probed with antibodies against DRC subunits and tektin. Loss or truncation of DRC2 was

the rescued strains (Figure 4A). The spectral counting data indicate that the DHC defects in *ida6* are much more extensive than previously reported (Kato *et al.*, 1993), but similar to the DHC defects observed in *pf3* (Bower *et al.*, 2013; Wirschell *et al.*, 2013).

Western blots of isolated axonemes probed with antibodies to several inner arm subunits confirmed these overall trends (Figures 3A and 4B). No obvious differences in the levels of outer arm (IC2) or I1 dynein subunits (IC140 and IC138) were observed in *ida6* axonemes. Similarly, DHC5 levels were not noticeably affected. However, the intermediate and light chains (p44, p38, p28) associated with IDAs *a*, *c*, and *d* (DHC6, DHC9, and DHC2) were slightly decreased in *ida6*, and DHC11 was slightly increased in *ida6*, consistent with the spectral counting data (Figures 3A and 4B).

Cryo–electron tomography (cryo-ET) has demonstrated that the N-DRC is closely connected to the base of RS2 and the CSC that interconnects RS2 with the neighboring short RS3 (RS3S) (Dymek *et al.*, 2011; Heuser *et al.*, 2012b). We therefore analyzed the iTRAQ data for possible changes in RS and CSC subunits to identify other polypeptides that might potentially interact with the N-DRC. No statistically significant differences were observed for most RS subunits, with the exception of RSP8, CaM-IP4/FAP251, and CaM-IP2/FAP91, which were reduced in both *ida6* and *pf3* (Table 2). Western blots of isolated axonemes confirmed that most RS subunits were unchanged in *ida6*, except for a consistent decrease in RSP8 (Figure 4C). Variable results were observed for CaM-IP3/FAP61 (aka as RSP19). CaM-IP3/FAP61 was significantly reduced in both *ida6* and *pf3* in only one of the two iTRAQ experiments (Table 2). However, multiple Western blots probed with antibodies against CaM-IP3 suggested that CaM-IP3 was reduced in *sup-pf5*, *ida6*, and *pf3* axonemes, but increased to WT levels in rescued strains (Figures 1E, 3A, and 4C). Analysis of the iTRAQ data also identified four other polypeptides that were reduced in *ida6* and *pf3* (Table 2). Most are not well characterized, but one protein, FAP206, was previously described as a conserved polypeptide whose phosphorylation state was altered in several *drc* mutants (Lin *et al.*, 2011). FAP206 is also missing in the RS mutant *pf14* (Lin *et al.*, 2011) and coimmunoprecipitates with the docking protein RSP3 (Gupta *et al.*, 2012). Recent study of a *fap206* mutant in *Tetrahymena* has shown that FAP206 is a docking protein for RS2 (Vasudevan *et al.*, 2015). Taken together, these observations and the reductions in CaM-IP3, CaM-IP4, RSP8, and FAP206 seen in *ida6* and *pf3* strongly suggest that the connections between the base of the N-DRC, the base of RS2, and the CSC might be destabilized in these two *drc* mutants.

Fractionation of N-DRC subunits in drc2 and drc4 mutants

Previous work demonstrated that N-DRC subunits are tightly bound to the outer doublet microtubules (Piperno *et al.*, 1994; Bower *et al.*, 2013). Following extraction by 04–0.6 M NaI and dialysis to lower ionic strength, most N-DRC subunits cosediment as a large complex on sucrose density gradients, but some subunits can dissociate from the larger complex, depending on buffer conditions or mutant background (Bower *et al.*, 2013; Wirschell *et al.*, 2013; Awata *et al.*,

2015). We therefore analyzed the solubility and sedimentation behavior of N-DRC subunits in *ida6* and *sup-pf5* extracts. As shown in Figure 5A, DRC4 could be extracted from *ida6* and *sup-pf5* axonemes with 0.6 M NaCl, but required 0.4–0.6 M NaI for extraction from WT or rescued strains. Thus, the absence of DRC2 (and DRC1) subunits in *ida6* and *sup-pf5* axonemes appeared to destabilize the association of DRC4 with the outer doublets. Similar results were observed with *drc4* mutant *pf2*. Both DRC1 and DRC2 could be readily extracted from *pf2* axonemes with 0.6M NaCl, but following rescue of *pf2* with DRC4-GFP, both DRC1 and DRC2 became more resistant to extraction with 0.6M NaCl (Figure 5A). These results indicated that the absence of DRC2 weakens the binding of DRC4 to the outer doublet and vice versa, even though neither subunit requires the other for assembly.

To determine how loss or truncation of DRC2 influences the stability of the isolated N-DRC, we analyzed DRC-containing extracts on sucrose density gradients (Figure 5). When extracts were prepared from either WT or *pf14* axonemes, most N-DRC subunits sedimented as a large complex near the bottom of the gradient, although a significant fraction of both DRC7 and DRC3 was sometimes observed closer to the top of the gradient (Figure 5, B and E). This pattern is similar to that seen previously with extracts from *DRC4-HA* and *DRC5-HA* rescued strains (Bower *et al.*, 2013). However, when extracts were prepared from either *ida6* or *sup-pf5* axonemes lacking DRC1 and DRC2, all of the DRC3, DRC4, and DRC7 subunits sedimented near the top of the gradient. In contrast, RSP16 still sedimented at ~20S, demonstrating that the RS were largely intact in these *drc* mutants (Figure 5, C and D). In extracts prepared from a *DRC2-HA* rescued strain, most N-DRC subunits reassociated and cosedimented as part of a larger complex, although a portion of DRC3 and DRC7 still sedimented at the top of the gradient (Figure 5F). These observations demonstrate that DRC1 and DRC2 are important for maintaining the integrity of the isolated N-DRC and further suggest that the N-DRC may be assembled in vivo from smaller sub-complexes (see the *Discussion*).

Cryo–electron tomography reveals defects in the assembly of multiple substructures

Analysis of WT and mutant axonemes by thin section TEM and 2D image averaging of longitudinal sections indicated that the crescent-shaped N-DRC structure was missing in *ida6* (Austin-Tse *et al.*, 2013). To obtain a clearer view of the impact of the *ida6* mutation on all the substructures within the axoneme, we reanalyzed the WT, *pf3*, *ida6*, and *DRC2-GFP* rescued strains by cryo-ET. Subtomogram averaging of 300–800 axonemal repeats per strain resulted in three-dimensional (3D) structures with resolution 3-4 nm and revealed significant defects in the assembly of multiple substructures (Figure 6, A–T).

Closer examination of the N-DRC demonstrated that *ida6* axonemes lack most of the region on the underside of the A-tubule known as the base plate (Figure 6, M–T). A defect in the base plate was previously observed only in *pf3* axonemes (Figure 6, N and R; see also Heuser *et al.*, 2009). The loss of this region is consistent

---

correlated with major decreases in DRC1 and tektin (see also Figure 1E), but changes in DRC4 were less obvious. DRC1 and tektin were increased to WT levels in *DRC2*-rescued strains. (A portion of the blot shown in E was previously shown in Austin-Tse *et al.*, 2013.) (G) A WT cell was mated to an *ida6* strain that had been rescued with *DRC2-GFP*, and the resulting quadriflagellate dikaryon was fixed 60 min after mating and viewed by DIC (left) and fluorescence (right) microscopy. GFP signal was visible in the two *DRC2-GFP* flagella but not in the two flagella from the WT parent. (H) An *ida6* cell was mated to an *ida6* strain that had been rescued with *DRC2-GFP*, and the resulting quadriflagellate dikaryon was fixed 30 min after mating and viewed by DIC (left) and fluorescence (right) microscopy. GFP signal was visible in all four flagella. All scale bars are 5 μm.

Protein	8-plex experiment					4-plex experiment		
	Peptides	WT/WT	*ida6*/WT	HA/WT	*pf3*/WT	Peptides	HA/HA	*ida6*/HA
DRC subunits								
DRC1	17 (22)	0.98	**0.29**	0.97	**0.29**	36 (92)	1.10	**0.31**
DRC2 (FAP250)	11 (14)	1.01	**0.29**	1.03	**0.31**	25 (50)	1.12	**0.31**
DRC3 (FAP134)	11 (8)	0.98	**0.50**	1.08	**0.44**	48 (79)	1.04	**0.51**
DRC4 (PF2)	16 (35)	0.96	**0.57**	0.96	**0.44**	69 (112)	1.00	**0.57**
DRC5 (FAP155)	2 (8)	1.01	**0.25**	0.97	**0.27**	17 (24)	0.97	**0.32**
DRC6 (FAP169)	5 (9)	1.01	**0.35**	1.06	**0.41**	21 (34)	1.09	**0.21**
DRC7 (FAP50)	32 (59)	1.01	**0.40**	0.83	**0.37**	103 (205)	1.03	**0.67**
DRC8 (FAP200)	5 (6)	0.95	**0.22**	0.88	**0.26**	10 (29)	1.18	**0.24**
DRC9 (FAP122)	12 (28)	1.03	**0.50**	1.02	**0.43**	33 (50)	1.03	**0.61**
DRC10 (FAP84)	4 (16)	1.03	**0.58**	0.94	**0.48**	20 (40)	1.06	**0.59**
DRC11 (FAP82)	19 (24)	0.97	**0.35**	0.87	**0.33**	63 (117)	1.02	**0.38**
MT doublet proteins								
Tektin*	29 (49)	1.00	**0.42**	0.91	**0.56**	46 (105)	1.08	**0.22**
CCDC39 (FAP59)	24 (46)	0.98	0.86	0.87	0.87	60 (107)	1.08	**1.21**
CCDC40 (FAP172)	31 (31)	0.96	0.87	0.82	**0.68**	74 (127)	1.09	**1.24**
Rib72	100 (146)	0.97	0.90	0.79	**0.82**	170 (259)	0.97	1.07
Rib43	34 (42)	1.00	0.90	0.93	0.85	41 (77)	1.09	1.13
PACRG	36 (72)	1.02	1.04	0.98	1.02	57 (161)	1.01	**1.13**
MBO2	20 (28)	1.04	**0.88**	0.90	0.78	73 (110)	1.06	**1.22**
FAP20	12 (15)	1.18	0.93	0.86	1.09	24 (44)	0.98	1.11
TUB	502 (892)	1.04	1.06	1.07	0.95	534 (1344)	0.95	0.98
TUA	343 (465)	1.02	0.94	0.93	1.07	517 (1390)	1.06	1.03
Radial spokes/CSC								
RSP1	69 (61)	0.99	0.88	0.99	0.94	88 (203)	1.17	1.12
RSP2	41 (35)	0.95	0.79	0.90	0.82	102 (158)	1.17	1.12
RSP3	41 (64)	0.97	0.87	1.00	0.84	65 (114)	1.09	1.09
RSP4	17 (15)	0.97	0.75	0.77	0.77	42 (75)	1.10	1.05
RSP5	19 (32)	0.86	**0.65**	0.76	0.65	53 (135)	1.05	1.07
RSP6	8 (18)	1.01	0.87	0.80	0.88	40 (40)	0.94	0.88
RSP7	29 (25)	0.97	0.84	0.95	0.87	53 (64)	1.03	**1.80**
RSP8*	7 (17)	0.99	**0.55**	0.96	0.61	22 (49)	1.04	**0.51**
RSP9	21 (29)	1.06	0.83	0.84	0.90	55 (98)	0.93	1.06
RSP10	1 (3)	1.06	0.98	1.03	1.07	23 (30)	1.10	1.18
RSP11	4 (8)	0.99	0.87	0.96	0.83	26 (37)	0.98	1.10
RSP12	2 (4)	0.99	0.84	0.94	0.86	15 (15)	1.06	1.28
RSP14	6 (27)	1.00	1.05	1.01	1.08	18 (49)	1.02	**1.35**
RSP16	30 (58)	0.96	0.82	0.89	0.81	58 (112)	1.13	1.21
RSP17	26 (26)	0.99	**0.70**	**0.84**	**0.67**	61 (95)	1.07	0.88
RSP19/CaM-IP3/FAP61	11 (15)	1.00	**0.55**	0.87	**0.53**	27 (49)	1.00	0.92
RSP20/CaM	7 (5)	0.88	0.67	1.05	0.73	36 (47)	1.00	0.89
RSP22/LC8	15 (46)	0.98	0.78	0.82	0.91	34 (67)	1.04	0.92
RSP23/NDK	16 (24)	0.94	0.85	0.98	0.87	37 (65)	1.09	1.21

TABLE 2: iTRAQ protein ratios in WT and *drc* mutant axonemes.

Protein	8-plex experiment					4-plex experiment		
	Peptides	WT/WT	*ida6*/WT	HA/WT	*pf3*/WT	Peptides	HA/HA	*ida6*/HA
CaM-IP4/FAP251*	19 (18)	1.03	**0.72**	0.91	0.81	26 (56)	0.99	**0.79**
CaM-IP2/FAP91*	18 (27)	0.96	**0.53**	0.94	**0.50**	38 (84)	1.04	**0.73**
FAP206*	16 (31)	0.99	**0.57**	0.92	**0.54**	20 (56)	0.98	**0.72**
Other								
FAP241*	14 (18)	0.93	**0.55**	0.88	**0.61**	32 (63)	1.09	**0.59**
FAP273*	11 (10)	1.02	**0.71**	0.90	0.99	17 (25)	1.06	**0.76**
Cre09.g397993*	11 (9)	0.99	**0.54**	0.77	0.54	19 (41)	1.04	**0.55**

The amount of protein in each sample was compared with that present in WT (or HA rescued sample) to obtain a protein ratio. The WT/WT and HA/HA ratios indicate the variability in iTRAQ labeling and protein loading between replicates of the same sample (typically less than 10%). For each protein, duplicate mutant/WT ratios were averaged, and those ratios that were statistically significant ($p < 0.05$) in both samples are indicated in bold. Peptides indicate the number used for protein ID (95% confidence) followed by the number used for iTRAQ quantification (in parentheses). Non-DRC subunits that are significantly reduced in *ida6* in both the 8-plex and the 4-plex iTRAQ experiments are indicated in bold type with an asterisk (*).

TABLE 2: iTRAQ protein ratios in WT and *drc* mutant axonemes. Continued

with the observations that DRC1 and DRC2 are uniquely missing in *pf3*, *sup-pf5*, and *ida6* (Figure 3; see also Bower et al., 2013). However, significant defects were also observed in the assembly of the linker region in *ida6* and *pf3* (Figure 6, J, K, and Q–T). The latter is

consistent with the decreases observed in most of the other DRC subunits (Figure 3A and Table 2). Only a small region at the base of the linker remains (Figure 6, J, K, R, and S), consistent with the presence of residual DRC4 in *pf3* and *ida6* (Figure 3A).
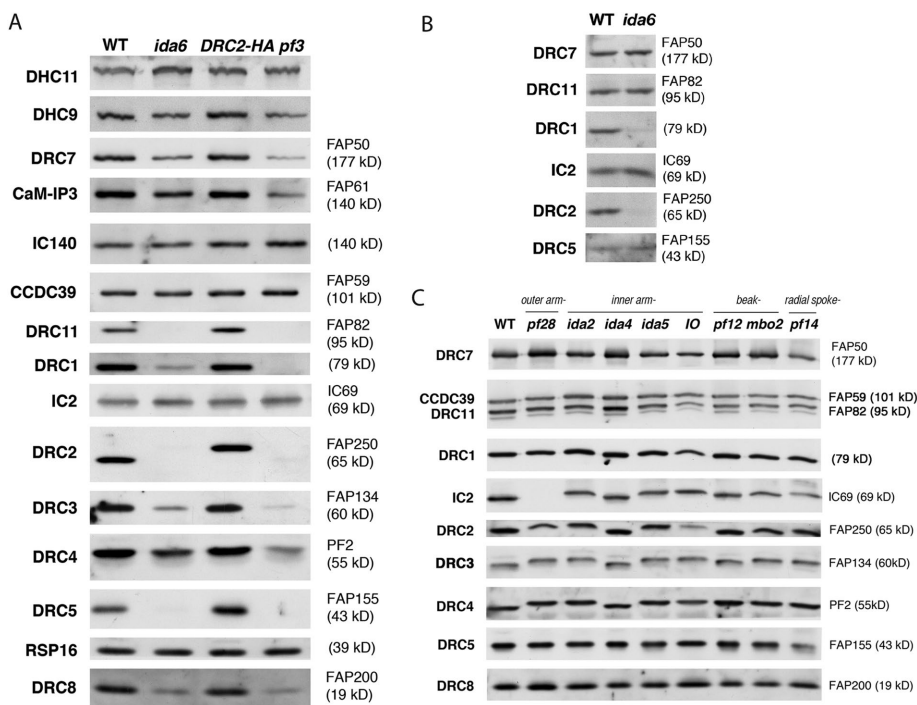

FIGURE 3: The distribution of N-DRC subunits in different strains identifies *ida6(drc2)* and *pf3(drc1)* as members of a distinct subclass of motility mutants. (A) Western blot of axonemes isolated from WT, *ida6, DRC2-HA,* and *pf3* strains was probed with multiple antibodies against DRC subunits and other axonemal proteins. DRC1, DRC2, DRC5, and DRC11 were clearly reduced or missing in *ida6* and *pf3*. DRC3, DRC4, DRC7, DRC8, and CaM-IP3 were slightly reduced. All were restored to WT levels in the *DRC2-HA* rescued strain. Subunits of the ODA (IC2/IC69), the I1 dynein (IC140), the RS (RSP16), and other doublet microtubule-associated proteins (FAP59) served as loading controls and were not noticeably altered in any strain. (B) Western blot of whole cell lysates obtained from WT and *ida6* cells was probed with antibodies against several DRC subunits. Both DRC1 and DRC2 were reduced in *ida6* cell lysates, but DRC5, DRC7, and DRC11 were present at WT levels in *ida6*. (C) Western blot of WT and motility mutants that disrupt other axoneme substructures (outer arms, inner arms, B-tubule beaks, and radial spokes) was probed with multiple antibodies against DRC subunits. FAP59/CCDC39 and IC69/IC2 served as loading controls.

The loss of the base plate also correlated with the loss of the "hole" seen at the A/B-tubule inner junction in WT axonemes (Figure 6, M–P). The hole was "filled" in *pf3* and *ida6* axonemes, but reappeared in the *DRC2-GFP* rescued axonemes. Most of the proteins associated with this region of the outer doublet are unknown, but the hole is located in close proximity to the protofilament ribbon recently observed near the A/B-tubule partition (Linck et al., 2014) and the inner junction protein FAP20 (Yanagisawa et al., 2014). No defects were observed in the assembly of ribbon proteins or FAP20 in either *pf3* or *ida6* (Table 2). However, tektin is reduced in *pf3, ida6, sup-pf5,* and the *fap20 (bug22)* mutant (Figures 1–3; see also Yanagisawa and Kamiya, 2004; Yanagisawa et al., 2014).

We also observed defects in the assembly of multiple IDA structures in *ida6* axonemes (Figure 6). As expected, inner arm IA4 corresponding to dynein *e* (DHC8) was missing in both *pf3* and *ida6* and restored in the *DRC2-GFP* rescued strain (Figure 6, A–L). This IDA is directly associated with the N-DRC (Gardner et al., 1994; Heuser et al., 2009). Two other inner arm structures closely associated with the N-DRC, IA5 (corresponding to dynein *g* or DHC7) and IA6 (corresponding to dynein *d* or DHC2), were also reduced in both *pf3* and *ida6* (Figure 6, B, C, F, G, J, and K). We also noted a decrease in intensity of the IA2 structure in *ida6* (Figure 6, C and G). IA2 (corresponding to dynein *a* or DHC6) is located in close proximity to RS1, well separated from both RS2 and the N-DRC. In addition, the decrease in IA2 seen in the *ida6* tomograms
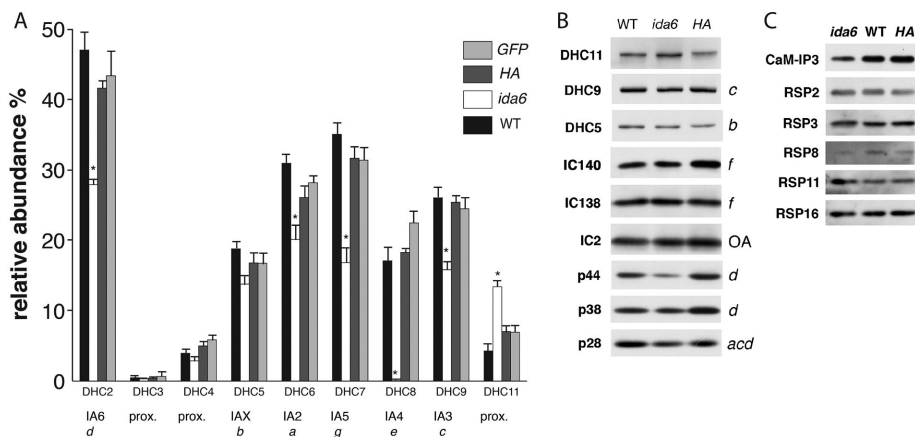
FIGURE 4: The assembly of a subset of IDA and RS subunits is altered in *ida6*. (A) The inner arm DHCs present in axonemes isolated from WT, *ida6*, and *DRC2* rescued strains (HA- and GFP-tagged) were fractionated by SDS–PAGE, digested with trypsin, and analyzed by mass spectrometry. The total number of spectra for each DHC was compared with the total number of spectra for the 1-alpha and 1-beta DHCs of the I1 dynein in each sample. Significant decreases were observed in *ida6* for DHC2, DHC6, DHC7, DHC8, and DHC9. DHC11 was increased in *ida6*. All DHCs were restored to WT levels in the *DRC2* rescued strains. For each DHC, the alternate name (dynein *a–g*) and the proposed inner arm position (IA2-6/X or proximal minor dynein, see also Figure 6A) are listed. (B) Western blot of isolated axonemes from WT, *ida6*, and a *DRC2-HA* rescued strain was probed with antibodies to different dynein subunits. (C) Western blot of isolated axonemes from WT, *ida6*, and a *DRC2-HA* rescued strain was probed with antibodies to different RS subunits.

was consistent with the reduction in DHC6 observed by spectral counting (Figure 4A). The multiple DHC defects in conjunction with the reduction in tektin indicate that *drc2* mutations can have both local effects (e.g., defects in assembly of the N-DRC) and broader impacts (e.g., defects in the assembly of tektin and multiple IDAs) beyond the immediate vicinity of the N-DRC.

Heterogeneity in the assembly of the radial spokes and CSC

The base plate of the N-DRC connects to the base of RS2, RS3S, and the CSC (Heuser *et al.*, 2012b). Analysis of CSC knockdown strains has shown that the CSC interconnects the base of RS2 to the neighboring RS3S, and that defects in the assembly of the CSC subunits lead to misplacement of the RSs in the 96-nm repeat (Heuser *et al.*, 2012b; Urbanska *et al.*, 2015). In earlier studies of *pf3*, we also noted that RSs were misplaced in a subset of longitudinal sections (Gardner *et al.*, 1994). Yet when we averaged all of the 96-nm repeats in *pf3* or *ida6*, no obvious differences in the assembly of the RS or CSC were detected (Figure 6, I–P). These observations raised the possibility that the averaging procedure might be masking genuine variability in the assembly of RS and the CSC in *pf3* and *ida6* axonemes. We therefore reviewed the images of the RS in the individual tomograms for the WT, *pf3, ida6*, and rescued *DRC2-GFP* strain. As shown in Supplemental Figure S1, all of the 96-nm repeats in the WT and rescued strain show the highly ordered spacing of RS1 and RS2 (Supplemental Figure S1, A and D). In contrast, variable RS assembly was observed in a subset of *pf3* and *ida6* tomograms (Supplemental Figure S1, B and C). Several 96-nm repeats lacked RS2, whereas other 96-nm repeats contained extra RSs at irregular positions. The tomograms were therefore sorted automatically into two different classes using the PEET software (Heumann *et al.*, 2011) and separately averaged into one class with regular RS repeats (~75%) and a second class with irregular RS repeats (~25%) (Figure 7). The class averages revealed that most of the 96-nm repeats in *pf3* and *ida6* assembled both

RS2 and RS3S at the appropriate position. However, the class averages of the tomograms containing irregular repeats showed that RS2 was missing and RS3S was reduced in both *pf3* and *ida6*. These results, together with the observation that some RS and CSC subunits are reduced in *pf3* and *ida6*, are consistent with the hypothesis that DRC1 and DRC2 stabilize connections to the CSC, RS2 and RS3S.

DISCUSSION

The impact of mutations in the DRC2 polypeptide

The N-DRC is a large, multisubunit complex critical for the regulation of ciliary motility, but little is known about the specific function of each subunit. Here we analyzed the phenotypes of two *drc2* mutant alleles in detail. DRC2 is a coiled-coil protein that extends from one end of the N-DRC linker to the opposite end of the base plate (Oda *et al.*, 2015). The *ida6* mutation is a single–base pair change in the stop codon that results in the addition of 101 amino acids to the DRC2 sequence (Figure 1). The mutant DRC2 polypeptide cannot assemble into the axoneme (Austin-Tse *et al.*, 2013), and the assembly of several other N-DRC subunits is reduced (Table 2; Figure 3). However, the addition of an HA (45 amino acids) or GFP (244 amino acids) tag to the C-terminus does not interfere with the ability of these constructs to rescue *ida6* and restore all the missing polypeptides and structures (Figures 2, 4, and 6). Therefore, increasing the length of DRC2 does not by itself inhibit DRC2 assembly. However, the additional 101 amino acids in *ida6* significantly increase the predicted isoelectric point of the DRC2 protein. Such a change could interfere with the preassembly of the N-DRC complex in the cytoplasm, its transport into the flagellar compartment, or its binding to the axoneme. The C-terminal half of the DRC2 polypeptide clearly plays a role in the attachment of the N-DRC to the outer doublet. Truncation of DRC2 as seen in *sup-pf5* reduces the amount of DRC2 and several other N-DRC subunits in the axoneme (Figure 1E). Given that the *sup-pf5* mutation is very close to the site of the *drc2/ccdc65* mutation found in several families with PCD (Figure 1D; see also Austin-Tse *et al.*, 2013; Horani *et al.*, 2013), the *sup-pf5* results suggest that the assembly of multiple N-DRC subunits is compromised in the respiratory cilia of the PCD patients.

Coassembly of DRC1 and DRC2 in the base plate of the N-DRC

Our experiments further demonstrate that DRC2 coassembles with DRC1 to form the N-DRC base plate on the A-tubule of the outer doublet. Loss or truncation of DRC2 inhibits the assembly of DRC1, and loss of DRC1 inhibits the assembly of DRC2 (Table 2; Figures 1–3). In addition, DRC2 and DRC1 cosediment as a subcomplex in extracts prepared from WT (Figure 5) and other *drc* mutant axonemes (e.g., *pf2, sup-pf3, sup-pf4* as described in Bower *et al.*, 2013). However, another component of the N-DRC base plate, DRC4, is still present in both *drc2* and *drc1* mutant axonemes (Figures 1 and 3 and Table 2; Song *et al.*, 2015). Moreover, even though DRC4 extends from the bottom of the base plate to the tip
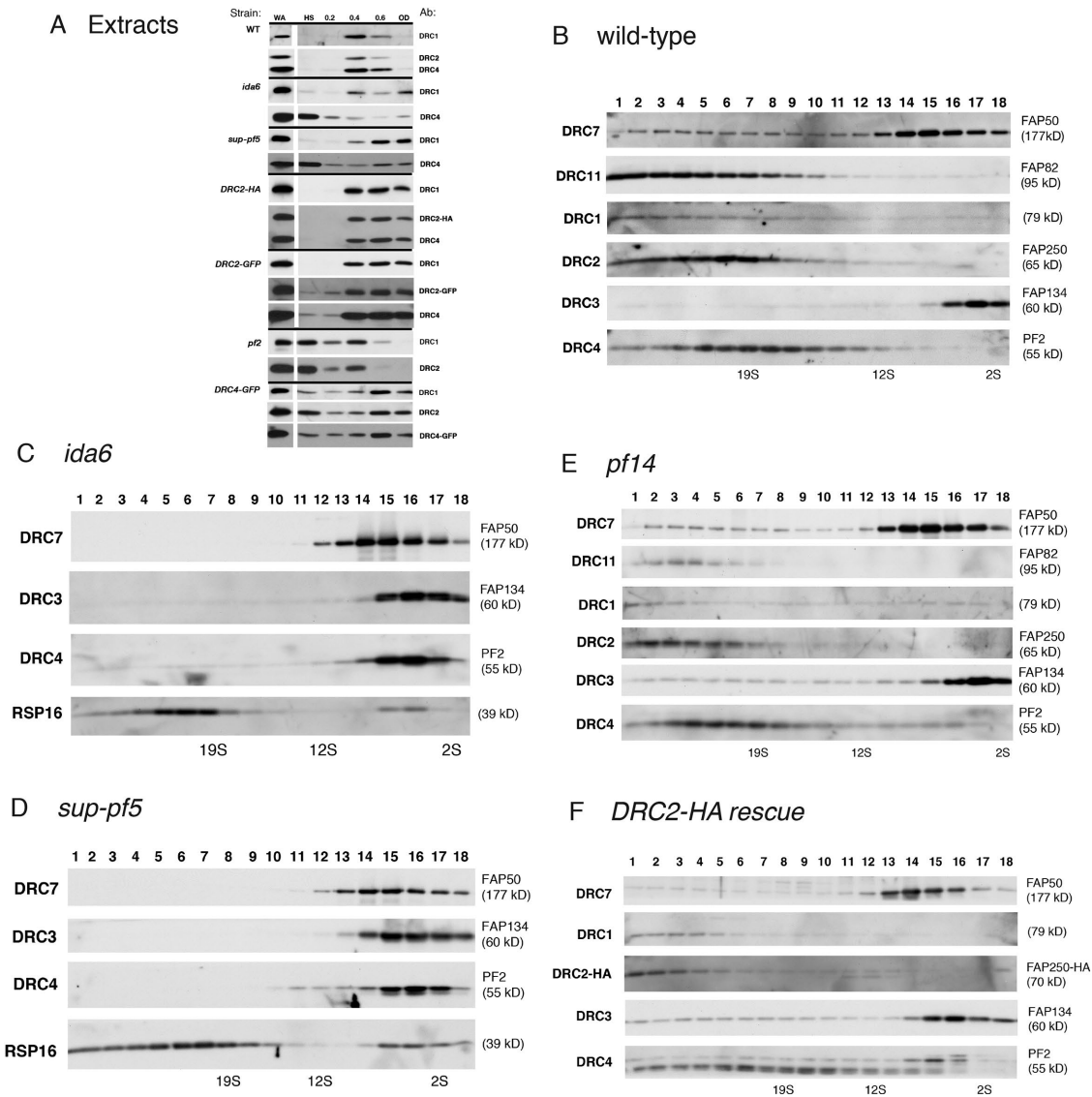
FIGURE 5: DRC1 and DRC2 form a distinct subcomplex whose loss alters the extraction or sedimentation behavior of other subunits of the N-DRC. (A) Whole axonemes (WA) were isolated from WT, three *drc* mutants (*ida6, sup-pf5,* and *pf2*), and three rescued strains (*ida6* rescued with *DRC2-HA* or *DRC2-GFP* and *pf2* rescued with *DRC4-GFP*) and then subjected to sequential extraction with 0.6 M NaCl (HS), followed by 0.2, 0.4, and 0.6 M NaI. The resulting extracts and final pellets of outer doublets (OD) were analyzed on Western blots probed with antibodies to DRC subunits. Note that DRC4 is more readily extracted from isolated axonemes in the absence of DRC1 and DRC2 and vice versa. (B–F) NaI extracts (0.5 M) of axonemes from WT (B), *ida6* (C), *sup-pf5* (D), *pf14* (E), and an *ida6* strain rescued with *DRC2-HA* (F) were fractionated by sucrose density gradient centrifugation and analyzed on Western blots probed with antibodies to different DRC subunits. Note the changes in sedimentation behavior of other DRC subunits, especially DRC4, in the absence of DRC1 and DRC2 in *ida6* and *sup-pf5.*

of the linker region (Oda *et al.*, 2015; Song *et al.*, 2015), the loss of DRC4 in the *pf2* mutant does not significantly affect the assembly of DRC1, DRC2, the base plate, or other nearby structures (Heuser *et al.*, 2009; Lin *et al.*, 2011; Bower *et al.*, 2013; Awata *et al.*, 2015; Song *et al.*, 2015). Taken together, these observations suggest that DRC1 and DRC2 coassemble to form a central scaffold needed for assembly of the N-DRC and its attachment to the outer doublet.

DRC1 and DRC2 stabilize the assembly of multiple IDAs and the RS

Previous work showed that *pf3/drc1* and *ida6/drc2* axonemes lack dynein *e*/DHC8/IA4 (Kato *et al.*, 1993; Gardner *et al.*, 1994; Heuser

et al., 2009; Bui *et al.*, 2012; Wirschell *et al.*, 2013). Cryo-ET indicated that at least one other IDA structure (IA5) was reduced in *pf3/drc1* (Heuser *et al.*, 2009). Mass spectrometry and spectral counting further suggested that there might be defects in several other IDAs in *pf3* (Wirschell *et al.* 2013). Cryo-ET and spectral counting of *ida6* axonemes have now shown that not only the IDAs closest to the N-DRC are reduced (IA4/DHC8, IA5/DHC7, IA6/DHC2), but IA2/DHC6 is also decreased. In contrast, a minor dynein, DHC11, located in the proximal portion of the axoneme appears to be elevated in *ida6*. The position of DHC11 in the 96-nm axoneme repeat is unknown, but previous work has suggested that DHC11 can bind to sites normally occupied by the other inner arm DHCs
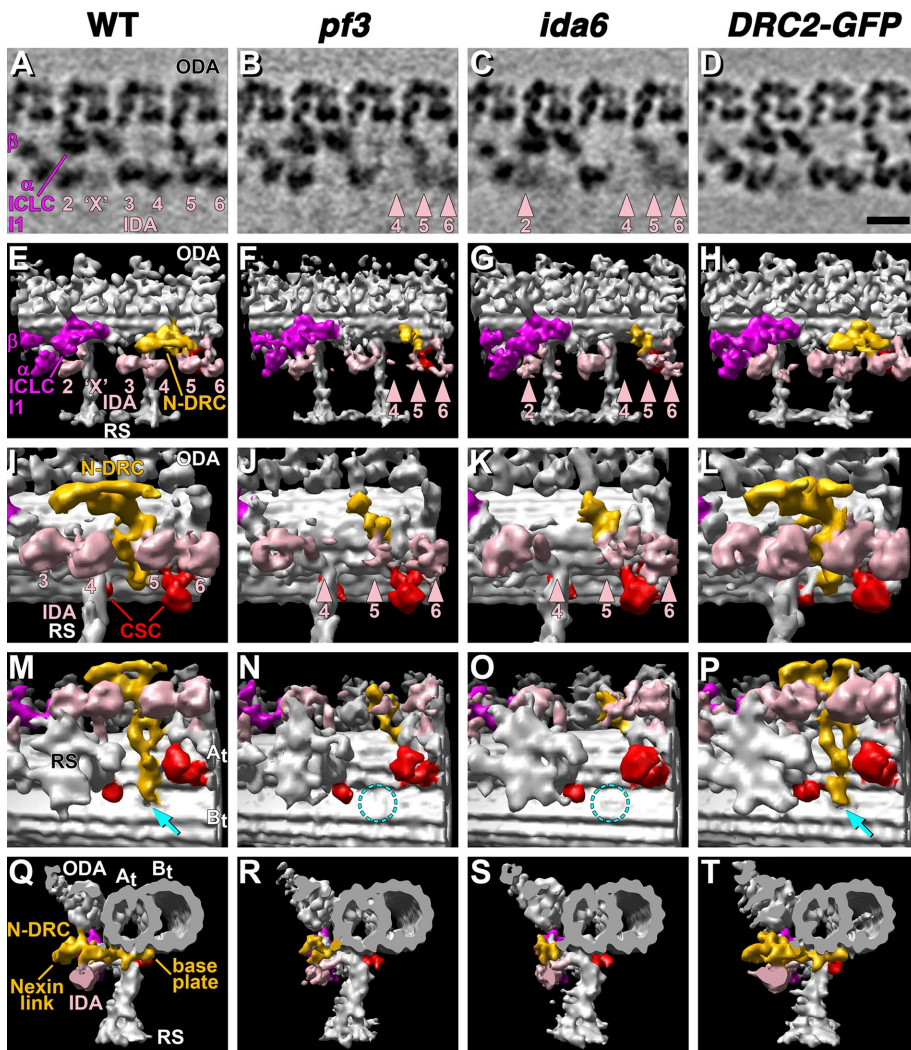
FIGURE 6: Cryo-ET reveals defects in the assembly of multiple structures in *ida6* and *pf3* axonemes. (A–T) Tomographic slices (A–D) and isosurface renderings (E–T) show the 3D structures of averaged 96-nm repeats of axonemes isolated from WT, *pf3* (*drc1*), *ida6* (*drc2*), and the *DRC2-GFP* rescued strain. Longitudinal views (A–P) show an overview of the entire repeat (A–H) and close-ups of the N-DRC (I–P) viewed from the front (E–L) and the bottom (looking from the CP toward the microtubule doublet, M–P). Cross-sectional views (Q–T) show the axonemal repeat viewed from the distal end of the N-DRC. Most structures, such as the ODAs or the I1 dynein, including α- and β-motor domains as well as the ICLC complex, appear very similar in all strains. However, some IDAs are reduced in both *drc* mutants: IA4 is missing, and IA5 and IA6 are reduced in both *pf3* and *ida6* (see rose arrowheads in B, C, F, G, J, K). Additionally, *ida6* shows a reduction in IA2 (C, G). Note that IAX is only present in a subset of doublets and is therefore more variable and weaker than the other IDAs (A–H). The N-DRC is severely reduced in both *drc* mutants: the linker region and most of the base plate are missing in *pf3* and *ida6,* and only a small portion of the N-DRC remains (J, K, N, O, R, S). In WT, the B-tubule has a small hole (*cyan arrow* in M) at the inner junction between the A- and B-tubules (A$_t$, B$_t$), which is not present in *pf3* and *ida6* (dashed cyan circles in N, O). All of the structural defects (IDAs, N-DRC, B-tubule hole) were repaired in the *DRC2-GFP* rescued strain, which appears indistinguishable from WT. The CSC (*red*) is located between the base of *RS2* and the shorter *RS3S* and shows no obvious differences in the averages of all repeats. Scale bar (D) is 20 nm. Similar views of the WT and *pf3* data were previously published (Heuser et al., 2009).

sembly of multiple IDAs, either directly by disrupting binding sites associated with the N-DRC or indirectly by altering the assembly of other proteins associated with the outer doublets (see below).

Recent studies of the CSC and FAP206 have shown that the three RS in each 96-nm repeat are structurally and biochemically distinct (Lin et al., 2012; Heuser et al., 2012b; Urbanska et al., 2015; Vasudevan et al., 2015). The CSC subunits link the base of RS2 with the base of RS3S (or RS3), and knockdown (by RNA interference [RNAi]) or knockout of CSC subunits and FAP206 result in defects in RS assembly (Heuser et al., 2012b; Urbanska et al., 2015; Vasudevan et al., 2015). We previously observed misplaced RS in a subset of *pf3* axonemes by thin-section TEM (Gardner et al., 1994). Following the identification of defects in the assembly of FAP206, RSP8, and several CSC subunits in both *pf3* and *ida6* axonemes by iTRAQ labeling and mass spectrometry (Table 2; Figure 4), we analyzed several *drc* mutants by cryo-ET to identify potential defects in RS assembly. Class averaging of *pf2* (*drc4*) tomograms showed no evidence of RS defects in any of the axoneme repeats. However, class averaging of *ida6* and *pf3* tomograms revealed that ~25% of the repeats had defects in the assembly of RS2 and RS3S. We predict that DRC1 and DRC2 interact directly or indirectly with FAP206 and CSC subunits near the base of the RS to stabilize the attachment of RS2 and RS3S to the axoneme, and that the reduction in FAP206 and CSC subunits is the primary cause for the heterogeneity in RS assembly observed in *pf3* and *ida6*.

The impact of drc1 and drc2 mutations on other components of the outer doublet microtubule

Tektins, Rib43, and Rib72 are the major components of the protofilament ribbon associated with the A-tubule of the outer doublet, and they are located in close proximity to protofilaments A11-A12-A13 or A12-A13-A1 (Linck et al., 2014). *Chlamydomonas* tektin is significantly reduced in *drc1* and *drc2* mutant axonemes (Yanagisawa and Kamiya, 2004; Austin-Tse et al., 2013; Wirschell et al., 2013) and restored to WT levels after rescue with the appropriate gene (Austin-Tse et al., 2013; this study, Figure 2 and Table 2). In addition, *tektin-t* mutations in

(Bui et al., 2012). Variable changes in DHC11 levels have also been observed in a subset of long flagella (*lf*) mutants (Sequeira et al., 2016). The factors that determine the levels and locations of each inner arm DHC are not well defined, but all of the DHCs affected in *ida6* are restored to WT levels in the *DRC2* rescued strains (Figures 4 and 6). Thus, the absence of DRC1 and DRC2 impacts the as-

mice have been linked to defects in the assembly of IDAs (Tanaka et al., 2004). Ikeda et al. (2003) proposed that the protofilament ribbon plays a role in templating the assembly of the N-DRC and other structures. More recent work has shown that the coiled-coil proteins CCDC39/FAP59 and CCDC40/FAP172 located on the surface of the A-tubule function as a molecular ruler to establish the spacing of the
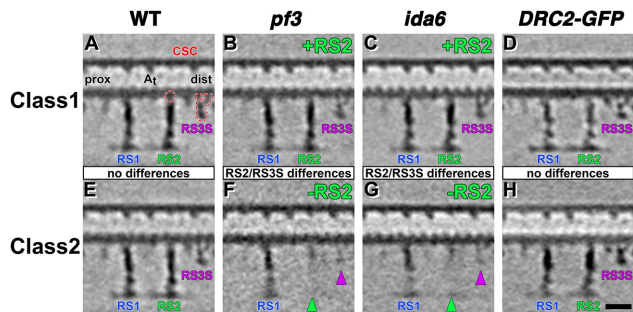
	WT	pf3	ida6	DRC2-GFP
Class1	A	B	C	D
Class2	E	F	G	H

FIGURE 7: Class averaging reveals defects in RS assembly in both *ida6* and *pf3* axonemes. A principal component–based classification of RS2 revealed heterogeneity in the 96-nm repeats of *pf3* and *ida6* axonemes (A–H). RS2 was present at its regular location in most 96-nm repeats but is missing from this site in ~25% of the repeats, and so the two classes of repeats were averaged separately. The tomographic slices show the center of the A-tubule (A_t) in longitudinal view. The proximal (prox) and distal (dist) ends of the repeats and the location of the CSC containing the base of RS2 and RS3S (outlined in red dashes) are shown in A for easier orientation. RS2 and RS3S are present in the Class 1 averages of *pf3* (B) and *ida6* (C) and look similar to WT (A). The Class 2 averages show that most of RS2 is missing (green arrowheads), except maybe a small remnant at the base, and RS3S is reduced (purple arrowheads) in both *pf3* (F) and *ida6* (G). In WT and the rescued *DRC2-GFP* strain, the classification approach yielded two almost identical classes without any RS defects. No defects in the assembly of RS1 were observed in any of the class averages. Scale bar (H) is 20 nm. See Supplemental Figure S1 for raw tomographic slices of intact axonemes showing the individual 96-nm repeats.

96-nm repeat (Oda *et al.*, 2014). Mutations in the *PF8* and *PF7* genes encoding these proteins destabilize the assembly of the RS, the N-DRC base plate, IDAs, and tektin (Oda *et al.*, 2014; Lin *et al.*, 2015). However, the identities of the specific adaptors for each structure remain unknown. iTRAQ analysis of several proteins previously associated with tektin (Ikeda *et al.*, 2003; Linck *et al.*, 2014; Oda *et al.*, 2014; Yanagisawa *et al.*, 2014) revealed no consistent changes in the levels of Rib43, Rib72, CCDC39, CCDC40, FAP20, or PACRG in either *drc1/pf3* or *drc2/ida6* axonemes (Table 2). In addition, we did not detect any obvious change in the structure of the outer doublets other than the filling of the "hole" located in the inner junction between A/B-tubule near the base of the N-DRC. Thus, the precise location of the tektin filament remains unresolved, although it seems likely that it adopts an extended conformation along the length of the 96-nm repeat, in close proximity to both CCDC39 and CCDC40 and the inner junction (Oda *et al.*, 2014; Yanagisawa *et al.*, 2014). We speculate that the tektin filament might also make contact with the base plate of the N-DRC. Such an arrangement could explain how defects in the N-DRC at the distal end of the 96-nm repeat might destabilize IDAs located in the more proximal region of the repeat. Further work to localize the tektin filament will be needed to test this hypothesis.

The impact of *drc1* and *drc2* mutations on flagellar and ciliary motility in *Chlamydomonas* and other species
The biochemical and structural phenotypes of *pf3*, *ida6*, and *sup-pf5* have revealed that mutations in DRC1 and DRC2 destabilize the assembly of multiple components in the *Chlamydomonas* axoneme (Figures 1–7). The *drc1* and *drc2* mutations also have profound effects on flagellar motility. Both forward swimming velocities and the shear amplitudes of the flagellar waveform are significantly reduced

(Figure 2; Brokaw and Kamiya, 1987; Kato *et al.*, 1993). The localization of DRC1 and DRC2 by epitope tagging and cryo-ET has further demonstrated that they coassemble in situ with DRC4 to form a central portion of the N-DRC extending from the base plate on the A-tubule through the linker region toward the neighboring B-tubule (Oda *et al.*, 2015; Song *et al.*, 2015). Disrupting this structure would be expected to reduce the resistance to dynein-driven microtubule sliding. In vitro studies of isolated axonemes and cell models have shown that mutations in *drc1*, *drc2*, and *drc4* inhibit reactivated motility and lead to the splaying of outer doublet microtubules (Bower *et al.*, 2013; Alford *et al.*, 2016). Measurements of flexural rigidity and shear stiffness in vanadate-treated axonemes have confirmed that elastic resistance is reduced in *pf3* axonemes (Xu *et al.*, 2016).

DRC1 and DRC2 are two of the most highly conserved and widely distributed N-DRC subunits in organisms with motile axonemes (Bower *et al.*, 2013; Nevers *et al.*, 2017). Given these observations and the central role of DRC1 and DRC2 in the assembly of the N-DRC described above, it is not surprising that *drc1* and *drc2* mutations have been linked to motility defects in other species. RNAi-mediated knockdown of DRC2 leads to motility defects in both trypanosome flagella and zebrafish cilia (Kabututu *et al.*, 2010; Austin-Tse *et al.*, 2013). Similarly, PCD causing mutations in CCDC164 (DRC1) and CCDC65 (DRC2) results in altered ciliary beat patterns in isolated respiratory cilia (Austin-Tse *et al.*, 2013; Horani *et al.*, 2013; Wirschell *et al.*, 2013). However, subtle defects in ciliary ultrastructure are very difficult to detect in images of axoneme cross-sections obtained by standard transmission electron microscopy in the absence of any computational averaging procedures (Austin-Tse *et al.*, 2013; Horani *et al.*, 2013; Wirschell *et al.*, 2013; Shapiro and Leigh, 2017). We predict that the PCD causing mutations in DRC1 and DRC2 likely disrupts the assembly of multiple axonemal substructures in human cilia similarly to that described here in *Chlamydomonas*. Additional structural studies of patient cilia by cryo-ET and computational averaging could be used to address this question.

Functions of other N-DRC subunits
Less is known about the specific functions of the other N-DRC subunits. Like DRC1 and DRC2, DRC3–DRC7 are structural proteins with coiled-coil or leucine-rich repeat domains predicted to be important for subunit interactions (Lin *et al.*, 2011; Bower *et al.*, 2013). DRC8–DRC11 also contain EF hand or IQ motifs predicted to bind calcium or calmodulin-like proteins (Bower *et al.*, 2013). They may interact with CSC and RS subunits, and play a role in calcium-mediated changes in flagellar motility, but their exact location in the N-DRC is still unknown.

The phenotypes of the *Chlamydomonas drc3* and *drc5/sup-pf4* mutations are subtle (see Table 1): forward swimming velocities are only slightly reduced, and small domains near the distal end of the linker region are missing (Heuser *et al.*, 2009; Bower *et al.*, 2013; Awata *et al.*, 2015). Mutations in the human orthologues for DRC3 (LRRC48) and DRC5 (TCTE1) have not yet been identified, but PCD-like symptoms have been observed in a mouse *Lrrc48* mutant with hydrocephalus, left–right laterality defects, sinusitis, and male infertility (Ha *et al.*, 2016), and *tcte1* mutations in mice have recently been associated with defects in sperm motility (Castaneda *et al.*, 2017). The *Chlamydomonas drc4* mutations (*pf2*, *sup-pf3*) primarily disrupt the N-DRC linker (Heuser *et al.*, 2009; Bower *et al.*, 2013), and the *pf2* motility defects are quite severe (Brokaw and Kamiya, 1987; Rupp and Porter, 2003; Bower *et al.*, 2013). Knockdown of DRC4 orthologues in trypanosomes, zebrafish, and mice results in severe motility defects (Hutchings *et al.*, 2002;

Colantonio et al., 2009; Lewis et al., 2016), and truncating mutations in the human gene (GAS8) have been linked to PCD (Olbrich et al., 2015; Jeanson et al., 2016; Lewis et al., 2016). The preliminary biochemical and structural characterization of gas8 cilia is consistent with defects in assembly of the N-DRC linker, as was observed previously for drc4 mutants in Chlamydomonas (Heuser et al., 2009; Bower et al., 2013).

No mutations in DRC6–DRC11 have yet been characterized in Chlamydomonas, but mutations in DRC7, DRC9, and DRC11 have been linked to motility defects in flies, mice, and trypanosomes, respectively (Yang et al., 2011; Nguyen et al., 2013; Harris et al., 2014; Li et al., 2014). Additional work is needed to localize each subunit within the substructure of the N-DRC and identify its specific function. Interestingly, comprehensive phylogenetic profiling has identified a subset of N-DRC subunits that are more widely distributed in organisms with motile axonemes than in others. For example, orthologues of DRC1, DRC2, DRC4, DRC7, and DRC11 are present in Thalassiosera (Nevers et al., 2017), a centric diatom with flagellated sperm and ODAs, but no IDAs, RS, or CP microtubules (Armbrust et al., 2004). One intriguing possibility is that these subunits represent a minimal functional core unit of the N-DRC required for regulation of dynein-driven microtubule sliding. Further study of the composition and structure of the N-DRC in organisms with more simplified axonemes may also provide new insights into the specific functions of N-DRC subunits.

MATERIALS AND METHODS

Culture conditions, genetic analyses, and strain construction
Strains used in this study are listed in Supplemental Table S1. Cells were maintained on Tris-acetate phosphate medium, but occasionally resuspended overnight in liquid minimal medium or 10 mM HEPES, pH 7.6, to facilitate flagellar assembly and mating. The site of the drc2 mutation in sup-pf5 was identified by PCR of genomic DNA and reverse transcriptase PCR (RT-PCR) of cDNA as previously described (Austin-Tse et al., 2013; Bower et al., 2013; see Supplemental Table S2). A genomic clone containing the full-length DRC2/FAP250 gene was subcloned from BAC 31n21 (Figure 1A; Austin-Tse et al., 2013). For the purpose of epitope tagging, a BglII site was created in the stop codon of the DRC2 gene using the Quick Change II XL mutagenesis kit (Stratagene) and the primers listed in Supplemental Table S2. A triple-HA epitope tag was amplified from the plasmid p3HA (gift of Carolyn Silflow, University of Minnesota), and a GFP tag was amplified from the pHisCrGFP plasmid (Fuhrmann et al., 1999) using the primers listed in Supplemental Table S2. Both tags were inserted into the BglII site and then sequenced to verify their orientation and sequence. The resulting changes in the DRC2 amino acid sequence are shown in Supplemental Table S2. All constructs were linearized with NotI prior to transformation.

Phase contrast and fluorescence microscopy, swimming velocities, and dikaryon rescues
Forward swimming velocities were assessed by phase contrast microscopy using a 40× objective on a Zeiss Axioskop as described by Bower et al. (2013). The distribution of DRC2-GFP in live cells immobilized in 1% low-melting-point agarose was analyzed using a Zeiss Axioskop with 100×, 1.3 N.A. Plan Neofluor objective, a CoolSNAP-ES monochrome CCD Camera (Photometrics), and the Metamorph software package, version 7.1.7.0 (Molecular Devices). Some images were collected on a Nikon Eclipse E800 photomicroscope using a 100×, 1.3 N.A. plan apo objective, a Photometrics Cascade 512B camera, and the ImagePro Plus software package available at the

University Imaging Center (University of Minnesota). Image stacks were collected using z-steps of 0.339 µm. For the image shown in Figure 2A, some sections were deconvolved using ImagePro Plus 6.2 Sharp Stack and then used to make a maximum intensity projection.

Cells or dikaryons were fixed using ice-cold methanol (Sanders and Salisbury, 1995) and stained for immunofluorescence using a mouse monoclonal antibody (mAb) to GFP (Molecular Probes) or a rat mAb to HA (Roche Clone 3F10) and an Alexafluor-488 conjugated secondary antibody (Molecular Probes; Mueller et al., 2005; Bower et al., 2013). Images were collected on the Zeiss Axioscop as described above. Selected images were cropped, rotated, and labeled in Adobe Photoshop.

Isolation of axonemes, fractionation of the N-DRC, SDS–PAGE, and Western blot analyses
Chlamydomonas whole cell lysates, isolated flagella, and demembranated axonemes were prepared as previously described (Witman, 1986; Bower et al., 2013; Reck et al., 2016). Purified axonemes were resuspended in HMEEN (10 mM HEPES, pH 7.4, 5 mM MgSO$_4$, 1 mM EGTA, 0.1 mM EDTA, 30 mM NaCl) plus 1 mM dithiothreitol (DTT) and 0.1 µg/ml protease inhibitors (leupeptin, aprotinin, pepstatin), and extracted with HMEEN containing 0.6 M NaCl or 0.2, 0.4, or 0.6 M NaI. N-DRC-containing extracts were dialyzed against HMEEN, clarified by centrifugation, and fractionated on 5–20% sucrose density gradients (Bower et al., 2013). Samples were separated on 5–15% polyacrylamide gradient gels, transferred to Immobilon P, and probed with different antibodies (Bower et al., 2013). Antibody sources and dilutions used are listed in Supplemental Table S3.

Preparation of samples for iTRAQ labeling and mass spectrometry
Isolated axonemes were washed briefly in 10 mM HEPES, pH 7.4, to remove salt, DTT, and protease inhibitors, resuspended in 0.5 M triethylammonium bicarbonate, pH 8.5, and processed for trypsin digestion and iTRAQ labeling as described in detail in Bower et al. (2013) and Reck et al. (2016). Samples were combined and fractionated offline using high-pH C18 reversed-phase chromatography (Reck et al., 2016). Column fractions were vacuum-dried, resuspended in solvent (98:2:0.01, water:acetonitrile:formic acid), and loaded in aliquots of 1–1.5 µg for capillary LC using a C18 column at low pH. The C18 column was mounted in a nanospray source directly in line with a Velos Orbitrap mass spectrometer (Thermo Fisher Scientific). Online capillary LC, MS/MS, database searching, and protein identification were performed as previously described (Lin-Moshier et al., 2013; Reck et al., 2016) using ProteinPilot software version 4.5 (AB Sciex) and the most recent version (v5.5) of the Chlamydomonas database (https://phytozome.jgi.doe.gov/pz/portal.html). The bias factors for all samples were normalized to alpha and beta tubulin (Reck et al., 2016).

Because the DHCs vary widely in abundance in isolated axonemes, not all inner arm DHCs were detected in both iTRAQ experiments. To improve the signal-to-noise for the DHCs, isolated axonemes were fractionated by SDS–PAGE and stained briefly with Coomassie blue, and the DHC region was excised from the gel (Bower et al., 2013). Following extraction and trypsin digestion, three to five replicates per sample were analyzed by tandem MS/MS. Both the total number of peptides and total number of assigned spectra per DHC isoform were analyzed. The relative abundance of each DHC was estimated by spectral counting (Zhu et al., 2010) and expressed as a percentage of the total spectra identified for the 1-alpha and 1-beta DHCs of the I1 dynein (Bower et al., 2013; Wirschell et al., 2013).

Cryo–electron tomography and image processing

Sample preparation, cryo-ET, and image processing were done as previously described (Nicastro *et al.*, 2006; Heuser *et al.*, 2009; Nicastro, 2009). Briefly, Quantifoil copper grids (Quantifoil Micro Tools, Jena, Germany) with a holey carbon film (R2/2, 200 mesh) were glow-discharged for 30 s at –40 mA and loaded with 3 μl of axoneme sample and 1 μl of 10-fold-concentrated 10 nm colloidal gold (Sigma-Aldrich). After brief mixing, grids were blotted from the front with filter paper for 2 s and plunge-frozen in liquid ethane using a homemade plunger. Vitrified samples were stored in liquid nitrogen and transferred to a Tecnai F30 transmission electron microscope (FEI) using a cryo holder (Gatan) for imaging. Single-axis tilt series of noncompressed, intact axonemes were acquired using the software package SerialEM (Mastronarde, 2005). Typically, 60–100 images were recorded at 13,500-fold magnification (~1 nm pixel size) with –6 to –8 μm defocus while the specimen was tilted from about –65° to +65° in 1.5–2.5° increments. The microscope was operated in low-dose mode at 300 keV and the accumulated electron dose of the sample was restricted to ~100 e/Å^2 to minimize radiation damage. Electron micrographs were recorded digitally with a 2 k × 2 k CCD camera (Gatan) after passing a post-column energy filter (Gatan) in zero-loss mode with a slit width of 20 eV.

The IMOD software package (Kremer *et al.*, 1996) was utilized to reconstruct tomograms from the recorded tilt series. The highly repetitive 96-nm repeat units of the axoneme were used for subtomogram averaging with the program PEET (Particle Estimation for Electron Tomography) (Nicastro *et al.*, 2006). At least 300–800 axonemal repeat units from two to six tomograms of each strain were aligned and averaged, resulting in 3D structures with compensated missing wedge effect, reduced noise, and thus increased resolution. The 3D averages for WT included four tomograms with 612 repeats, for *pf3* three tomograms with 500 repeats, for *ida6* six tomograms with 800 repeats, and for the *ida6* rescued strain (*DRC2-GFP*) two tomograms with 300 repeats. The 3D visualization of the averaged 96-nm repeat units was achieved by isosurface rendering with the UCSF Chimera package (Pettersen *et al.*, 2004) using the microtubule mass to normalize the isosurface-rendering threshold of all averages. Classification of RS2 used a principal component–based clustering analysis integrated into the PEET software package (Heumann *et al.*, 2011) and was performed as previously described (Heuser *et al.*, 2012b).

REFERENCES

Alford LM, Stoddard D, Li JH, Hunter EL, Tritschler D, Bower R, Nicastro D, Porter ME, Sale WS (2016). The nexin link and B-tubule glutamylation maintain the alignment of outer doublets in the ciliary axoneme. Cytoskeleton (Hoboken) 73, 331–340.

Armbrust EV, Berges JA, Bowler C, Green BR, Martinez D, Putnam NH, Zhou S, Allen AE, Apt KE, Bechner M, *et al.* (2004). The genome of the diatom *Thalassiosira pseudonana*: ecology, evolution, and metabolism. Science 306, 79–86.

Austin-Tse C, Halbritter J, Zariwala MA, Gilberti RM, Gee HY, Hellman N, Pathak N, Liu Y, Panizzi JR, Patel-King RS, *et al.* (2013). Zebrafish ciliopathy screen plus human mutational analysis identifies C21orf59 and CCDC65 defects as causing primary ciliary dyskinesia. Am J Hum Genet 93, 672–686.

Awata J, Song K, Lin J, King SM, Sanderson MJ, Nicastro D, Witman GB (2015). DRC3 connects the N-DRC to dynein *g* to regulate flagellar waveform. Mol Biol Cell 26, 2788–2800.

Blackburn K, Bustamante-Marin X, Yin W, Goshe MB, Ostrowski LE (2017). Quantitative proteomic analysis of human airway cilia identifies previously uncharacterized proteins of high abundance. J Proteome Res 16, 1579–1592.

Bower R, Tritschler D, Vanderwaal K, Perrone CA, Mueller J, Fox L, Sale WS, Porter ME (2013). The N-DRC forms a conserved biochemical complex that maintains outer doublet alignment and limits microtubule sliding in motile axonemes. Mol Biol Cell 24, 1134–1152.

Bower R, VanderWaal K, O'Toole E, Fox L, Perrone C, Mueller J, Wirschell M, Kamiya R, Sale WS, Porter ME (2009). IC138 defines a subdomain at the base of the I1 dynein that regulates microtubule sliding and flagellar motility. Mol Biol Cell 20, 3055–3063.

Brokaw CJ, Kamiya R (1987). Bending patterns of *Chlamydomonas* flagella: IV. mutants with defects in dynein arms indicate differences in dynein arm function. Cell Motil Cytoskeleton 8, 68–75.

Bui KH, Yagi T, Yamamoto R, Kamiya R, Ishikawa T (2012). Polarity and asymmetry in the arrangement of dynein and related structures in the *Chlamydomonas* axoneme. J Cell Biol 198, 913–925.

Castaneda JM, Hua R, Miyata H, Oji A, Guo Y, Cheng Y, Zhou T, Guo X, Cui Y, Shen B, *et al.* (2017). TCTE1 is a conserved component of the dynein regulatory complex and is required for motility and metabolism in mouse spermatozoa. Proc Natl Acad Sci USA 114, E5370–E5378.

Colantonio JR, Vermot J, Wu D, Langenbacher AD, Fraser S, Chen JN, Hill KL (2009). The dynein regulatory complex is required for ciliary motility and otolith biogenesis in the inner ear. Nature 457, 205–209.

Dymek EE, Heuser T, Nicastro D, Smith EF (2011). The CSC is required for complete radial spoke assembly and wild-type ciliary motility. Mol Biol Cell 22, 2520–2531.

Fox LA, Sale WS (1987). Direction of force generated by the inner row of dynein arms on flagellar microtubules. J Cell Biol 105, 1781–1787.

Fuhrmann M, Oertel W, Hegemann P (1999). A synthetic gene coding for the green fluorescent protein (GFP) is a versatile reporter in *Chlamydomonas reinhardtii*. Plant J 19, 353–361.

Gardner LC, O'Toole E, Perrone CA, Giddings T, Porter ME (1994). Components of a "dynein regulatory complex" are located at the junction between the radial spokes and the dynein arms in *Chlamydomonas* flagella. J Cell Biol 127, 1311–1325.

Gibbons IR (1965). Chemical dissection of cilia. Arch Biol (Liege) 76, 317–352.

Gupta A, Diener DR, Sivadas P, Rosenbaum JL, Yang P (2012). The versatile molecular complex component LC8 promotes several distinct steps of flagellar assembly. J Cell Biol 198, 115–126.

Ha S, Lindsay AM, Timms AE, Beier DR (2016). Mutations in Dnaaf1 and Lrrc48 cause hydrocephalus, laterality defects, and sinusitis in mice. G3 (Bethesda) 6, 2479–2487.

Harris TP, Schimenti KJ, Munroe RJ, Schimenti JC (2014). IQ motif-containing G (Iqcg) is required for mouse spermiogenesis. G3 (Bethesda) 4, 367–372.

Heumann JM, Hoenger A, Mastronarde DN (2011). Clustering and variance maps for cryo-electron tomography using wedge-masked differences. J Struct Biol 175, 288–299.

Heuser T, Barber CF, Lin J, Krell J, Rebesco M, Porter ME, Nicastro D (2012a). Cryoelectron tomography reveals doublet-specific structures and unique interactions in the I1 dynein. Proc Natl Acad Sci USA 109, E2067–2076.

Heuser T, Dymek EE, Lin J, Smith EF, Nicastro D (2012b). The CSC connects three major axonemal complexes involved in dynein regulation. Mol Biol Cell 23, 3143–3155.

Heuser T, Raytchev M, Krell J, Porter ME, Nicastro D (2009). The dynein regulatory complex is the nexin link and a major regulatory node in cilia and flagella. J Cell Biol 187, 921–933.

Horani A, Brody SL, Ferkol TW, Shoseyov D, Wasserman MG, Ta-shma A, Wilson KS, Bayly PV, Amirav I, Cohen-Cymberknoh M, et al. (2013). CCDC65 mutation causes primary ciliary dyskinesia with normal ultra-structure and hyperkinetic cilia. PLoS One 8, e72299.

Huang B, Piperno G, Luck DJ (1979). Paralyzed flagella mutants of Chlamydomonas reinhardtii defective for axonemal doublet microtubule arms. J Biol Chem 254, 3091–3099.

Huang B, Ramanis Z, Luck DJ (1982). Suppressor mutations in Chlamydomonas reveal a regulatory mechanism for flagellar function. Cell 28, 115–124.

Huang B, Rifkin MR, Luck DJ (1977). Temperature-sensitive mutations affect-ing flagellar assembly and function in Chlamydomonas reinhardtii. J Cell Biol 72, 67–85.

Hutchings NR, Donelson JE, Hill KL (2002). Trypanin is a cytoskeletal linker protein and is required for cell motility in African trypanosomes. J Cell Biol 156, 867–877.

Ikeda K, Brown JA, Yagi T, Norrander JM, Hirono M, Eccleston E, Kamiya R, Linck RW (2003). Rib72, a conserved protein associated with the rib-bon compartment of flagellar A-microtubules and potentially involved in the linkage between outer doublet microtubules. J Biol Chem 278, 7725–7734.

Ishikawa H, Thompson J, Yates JR 3rd, Marshall WF (2012). Proteomic analy-sis of mammalian primary cilia. Curr Biol 22, 414–419.

Jeanson L, Thomas L, Copin B, Coste A, Sermet-Gaudelus I, Dastot-Le Moal F, Duquesnoy P, Montantin G, Collot N, Tissier S, et al. (2016). Mutations in GAS8, a gene encoding a nexin-dynein regulatory complex subunit, cause primary ciliary dyskinesia with axonemal disorganization. Hum Mutat 37, 776–785.

Kabututu ZP, Thayer M, Melehani JH, Hill KL (2010). CMF70 is a subunit of the dynein regulatory complex. J Cell Sci 123, 3587–3595.

Kamiya R, Kurimoto E, Muto E (1991). Two types of Chlamydomonas flagel-lar mutants missing different components of inner-arm dynein. J Cell Biol 112, 441–447.

Kato T, Kagami O, Yagi T, Kamiya R (1993). Isolation of two species of Chlamydomonas reinhardtii flagellar mutants, ida5 and ida6, that lack a newly identified heavy chain of the inner dynein arm. Cell Struct Funct 18, 371–377.

Kremer JR, Mastronarde DN, McIntosh JR (1996). Computer visualization of three-dimensional image data using IMOD. J Struct Biol 116, 71–76.

Lewis WR, Malarkey EB, Tritschler D, Bower R, Pasek RC, Porath JD, Birket SE, Saunier S, Antignac C, Knowles MR, et al. (2016). Mutation of growth arrest specific 8 reveals a role in motile cilia function and human disease. PLoS Genet 12, e1006220.

Li JB, Gerdes JM, Haycraft CJ, Fan Y, Teslovich TM, May-Simera H, Li H, Blacque OE, Li L, Leitch CC, et al. (2004). Comparative genomics identi-fies a flagellar and basal body proteome that includes the BBS5 human disease gene. Cell 117, 541–552.

Li RK, Tan JL, Chen LT, Feng JS, Liang WX, Guo XJ, Liu P, Chen Z, Sha JH, Wang YF, Chen SJ (2014). Iqcg is essential for sperm flagellum formation in mice. PLoS One 9, e98053.

Lin H, Zhang Z, Guo S, Chen F, Kessler JM, Wang YM, Dutcher SK (2015). A NIMA-related kinase suppresses the flagellar instability associated with the loss of multiple axonemal structures. PLoS Genet 11, e1005508.

Lin J, Heuser T, Carbajal-Gonzalez BI, Song K, Nicastro D (2012). The struc-tural heterogeneity of radial spokes in cilia and flagella is conserved. Cytoskeleton (Hoboken) 69, 88–100.

Lin J, Tritschler D, Song K, Barber CF, Cobb JS, Porter ME, Nicastro D (2011). Building blocks of the nexin-dynein regulatory complex in Chlamydomonas flagella. J Biol Chem 286, 29175–29191.

Lin-Moshier Y, Sebastian PJ, Higgins L, Sampson ND, Hewitt JE, Marchant JS (2013). Re-evaluation of the role of calcium homeostasis endoplasmic reticulum protein (CHERP) in cellular calcium signaling. J Biol Chem 288, 355–367.

Linck R, Fu X, Lin J, Ouch C, Schefter A, Steffen W, Warren P, Nicastro D (2014). Insights into the structure and function of ciliary and flagellar doublet microtubules: tektins, Ca2+-binding proteins, and stable proto-filaments. J Biol Chem 289, 17427–17444.

Mastronarde DN (2005). Automated electron microscope tomography using robust prediction of specimen movements. J Struct Biol 152, 36–51.

Mastronarde DN, O'Toole ET, McDonald KL, McIntosh JR, Porter ME (1992). Arrangement of inner dynein arms in wild-type and mutant flagella of Chlamydomonas. J Cell Biol 118, 1145–1162.

Mitchell DR, Rosenbaum JL (1985). A motile Chlamydomonas flagellar mutant that lacks outer dynein arms. J Cell Biol 100, 1228–1234.

Mitchison HM, Valente EM (2017). Motile and non-motile cilia in human pathology: from function to phenotypes. J Pathol 241, 294–309.

Mizuno N, Taschner M, Engel BD, Lorentzen E (2012). Structural studies of ciliary components. J Mol Biol 442, 163–180.

Mueller J, Perrone CA, Bower R, Cole DG, Porter ME (2005). The FLA3 KAP subunit is required for localization of kinesin-2 to the site of flagellar assembly and processive anterograde intraflagellar transport. Mol Biol Cell 16, 1341–1354.

Nevers Y, Prasad MK, Poidevin L, Chennen K, Allot A, Kress A, Ripp R, Thompson JD, Dollfus H, Poch O, Lecompte O (2017). Insights into cili-ary genes and evolution from multi-level phylogenetic profiling. Mol Biol Evol 34, 2016–2034.

Nguyen HT, Sandhu J, Langousis G, Hill KL (2013). CMF22 is a broadly conserved axonemal protein and is required for propulsive motility in Trypanosoma brucei. Eukaryot Cell 12, 1202–1213.

Nicastro D (2009). Cryo-electron microscope tomography to study axone-mal organization. Methods Cell Biol 91, 1–39.

Nicastro D, Schwartz C, Pierson J, Gaudette R, Porter ME, McIntosh JR (2006). The molecular architecture of axonemes revealed by cryoelec-tron tomography. Science 313, 944–948.

Oda T, Yanagisawa H, Kamiya R, Kikkawa M (2014). A molecular ruler de-termines the repeat length in eukaryotic cilia and flagella. Science 346, 857–860.

Oda T, Yanagisawa H, Kikkawa M (2015). Detailed structural and biochemi-cal characterization of the nexin-dynein regulatory complex. Mol Biol Cell 26, 294–304.

Olbrich H, Cremers C, Loges NT, Werner C, Nielsen KG, Marthin JK, Phil-ipsen M, Wallmeier J, Pennekamp P, Menchen T, et al. (2015). Loss-of-function GAS8 mutations cause primary ciliary dyskinesia and disrupt the nexin-dynein regulatory complex. Am J Hum Genet 97, 546–554.

Pazour GJ, Agrin N, Leszyk J, Witman GB (2005). Proteomic analysis of a eukaryotic cilium. J Cell Biol 170, 103–113.

Pettersen EF, Goddard TD, Huang CC, Couch GS, Greenblatt DM, Meng EC, Ferrin TE (2004). UCSF chimera—a visualization system for explor-atory research and analysis. J Comput Chem 25, 1605–1612.

Piperno G (1995). Regulation of dynein activity within Chlamydomonas flagella. Cell Motil Cytoskeleton 32, 103–105.

Piperno G, Mead K, LeDizet M, Moscatelli A (1994). Mutations in the "dy-nein regulatory complex" alter the ATP-insensitive binding sites for inner arm dyneins in Chlamydomonas axonemes. J Cell Biol 125, 1109–1117.

Piperno G, Mead K, Shestak W (1992). The inner dynein arms I2 interact with a "dynein regulatory complex" in Chlamydomonas flagella. J Cell Biol 118, 1455–1463.

Portman N, Lacomble S, Thomas B, McKean PG, Gull K (2009). Combin-ing RNA interference mutants and comparative proteomics to identify protein components and dependences in a eukaryotic flagellum. J Biol Chem 284, 5610–5619.

Reck J, Schauer AM, VanderWaal Mills K, Bower R, Tritschler D, Perrone CA, Porter ME (2016). The role of the dynein light intermediate chain in retrograde IFT and flagellar function in Chlamydomonas. Mol Biol Cell 27, 2404–2422.

Reiter JF, Leroux MR (2017). Genes and molecular pathways underpinning ciliopathies. Nat Rev Mol Cell Biol 18, 533–547.

Rupp G, Porter ME (2003). A subunit of the dynein regulatory complex in Chlamydomonas is a homologue of a growth arrest-specific gene prod-uct. J Cell Biol 162, 47–57.

Sale WS, Satir P (1977). The direction of active sliding of microtubules in Tetrahymena cilia. Proc Natl Acad Sci USA 74, 2045–2049.

Sanders MA, Salisbury JL (1995). Immunofluorescence microscopy of cilia and flagella. Methods Cell Biol 47, 163–169.

Satir P (1968). Studies on cilia III. further studies on the cilium tip and a "slid-ing filament" model of ciliary motility. J Cell Biol 39, 77–94.

Satir P (1985). Switching mechanisms in the control of ciliary motility. Mod Cell Biol 4, 1–46.

Segal RA, Huang B, Ramanis Z, Luck DJL (1984). Mutant strains of Chlamydo-monas reinhardtii that move backwards only. J Cell Biol 98, 2026–2034.

Sequeira MP, Sinha S, Motiwalla MJ, Rao VG, D'Souza JS (2016). Defects in the ratio of dynein isoform, DHC11 in the long-flagella mutants of Chlam-ydomonas reinhardtii. Biochem Biophys Res Commun 482, 610–614.

Shapiro AJ, Leigh MW (2017). Value of transmission electron microscopy for primary ciliary dyskinesia diagnosis in the era of molecular medicine: genetic defects with normal and non-diagnostic ciliary ultrastructure. Ultrastruct Pathol 41, 373–385.

Smith EF (2002). Regulation of flagellar dynein by the axonemal central apparatus. Cell Motil Cytoskeleton 52, 33–42.

Smith EF, Sale WS (1992). Regulation of dynein-driven microtubule sliding by the radial spokes in flagella. Science 257, 1557–1559.

Smith EF, Yang P (2004). The radial spokes and central apparatus: mechano-chemical transducers that regulate flagellar motility. Cell Motil Cytoskeleton 57, 8–17.

Song K, Awata J, Tritschler D, Bower R, Witman GB, Porter ME, Nicastro D (2015). In situ localization of N and C termini of subunits of the glagellar nexin-dynein regulatory complex (N-DRC) using SNAP tag and cryo-electron tomography. J Biol Chem 290, 5341–5353.

Tam LW, Lefebvre PA (2002). The *Chlamydomonas MBO2* locus encodes a conserved coiled-coil protein important for flagellar waveform conversion. Cell Motil Cytoskeleton 51, 197–212.

Tanaka H, Iguchi N, Toyama Y, Kitamura K, Takahashi T, Kaseda K, Maekawa M, Nishimune Y (2004). Mice deficient in the axonemal protein tektin-t exhibit male infertility and immotile-cilium syndrome due to impaired inner arm dynein function. Mol Cell Biol 24, 7958–7964.

Urbanska P, Song K, Joachimiak E, Krzemien-Ojak L, Koprowski P, Hennessey T, Jerka-Dziadosz M, Fabczak H, Gaertig J, Nicastro D, Wloga D (2015). The CSC proteins FAP61 and FAP251 build the basal substructures of radial spoke 3 in cilia. Mol Biol Cell 26, 1463–1475.

Vasudevan KK, Song K, Alford LM, Sale WS, Dymek EE, Smith EF, Hennessey T, Joachimiak E, Urbanska P, Wloga D, *et al.* (2015). FAP206 is a microtubule-docking adapter for ciliary radial spoke 2 and dynein c. Mol Biol Cell 26, 696–710.

Wirschell M, Olbrich H, Werner C, Tritschler D, Bower R, Sale WS, Loges NT, Pennekamp P, Lindberg S, Stenram U, *et al.* (2013). The nexin-dynein regulatory complex subunit DRC1 is essential for motile cilia function in algae and humans. Nat Genet 45, 262–269.

Witman GB (1986). Isolation of *Chlamydomonas* flagella and flagellar axonemes. Methods Enzymol 134, 280–290.

Witman GB, Plummer J, Sander G (1978). *Chlamydomonas* flagellar mutants lacking radial spokes and central tubules. Structure, composition, and function of specific axonemal components. J Cell Biol 76, 729–747.

Wren KN, Craft JM, Tritschler D, Schauer A, Patel DK, Smith EF, Porter ME, Kner P, Lechtreck KF (2013). A differential cargo-loading model of ciliary length regulation by IFT. Curr Biol 23, 2463–2471.

Xu G, Wilson KS, Okamoto RJ, Shao JY, Dutcher SK, Bayly PV (2016). Flexural rigidity and shear stiffness of flagella estimated from induced bends and counterbends. Biophys J 110, 2759–2768.

Yamamoto R, Obbineni JM, Alford LM, Ide T, Owa M, Hwang J, Kon T, Inaba K, James N, King SM, *et al.* (2017). *Chlamydomonas* DYX1C1/PF23 is essential for axonemal assembly and proper morphology of inner dynein arms. PLoS Genetics 13, e1006996.

Yamamoto R, Song K, Yanagisawa HA, Fox L, Yagi T, Wirschell M, Hirono M, Kamiya R, Nicastro D, Sale WS (2013). The MIA complex is a conserved and novel dynein regulator essential for normal ciliary motility. J Cell Biol 201, 263–278.

Yanagisawa HA, Kamiya R (2004). A tektin homologue is decreased in *Chlamydomonas* mutants lacking an axonemal inner-arm dynein. Mol Biol Cell 15, 2105–2115.

Yanagisawa HA, Mathis G, Oda T, Hirono M, Richey EA, Ishikawa H, Marshall WF, Kikkawa M, Qin H (2014). FAP20 is an inner junction protein of doublet microtubules essential for both the planar asymmetrical waveform and stability of flagella in *Chlamydomonas*. Mol Biol Cell 25, 1472–1483.

Yang Y, Cochran DA, Gargano MD, King I, Samhat NK, Burger BP, Sabourin KR, Hou Y, Awata J, Parry DA, *et al.* (2011). Regulation of flagellar motility by the conserved flagellar protein CG34110/Ccdc135/FAP50. Mol Biol Cell 22, 976–987.

Zhu W, Smith JW, Huang CM (2010). Mass spectrometry-based label-free quantitative proteomics. J Biomed Biotechnol 2010, 840518.